J. Wind Eng. Ind. Aerodyn. 145 (2015) 42–60

Contents lists available at ScienceDirect

Journal of Wind Engineering and Industrial Aerodynamics

journal homepage: www.elsevier.com/locate/jweia

Numerical study of turbulent flow fields and the similarity of tornado vortices using large-eddy simulations

Zhenqing Liu [a,*], Takeshi Ishihara [b]

[a] School of Civil Engineering and Mechanics, Huazhong University of Science and Technology, Wuhan, Hubei, China
[b] Department of Civil Engineering, School of Engineering, The University of Tokyo, Tokyo, Japan

ARTICLE INFO

Article history:
Received 3 January 2014
Received in revised form
20 March 2015
Accepted 18 May 2015

Keywords:
Tornado vortex
LES
Swirl ratio
Turbulent flow fields
Force balance
Similarity

ABSTRACT

Tornado vortices are investigated using large-eddy simulations of a single vortex evolving into a multi-vortex. Four typical tornado configurations, including a weak vortex, a vortex breakdown, a vortex touchdown and a multi-vortex, are investigated to provide detailed information on the turbulent flow fields. The force balances in the radial and vertical directions are also evaluated using axsymmetrically and time averaged results. The local corner swirl ratio is used as an index to describe the surface intensification and the geometry of tornado vortices; the similarity between the simulated tornadoes and a full-scale tornado in nature is examined. Good agreements between the data of scaled tornado in simulation and the observed data of the full-scale tornado in nature are achieved.

1. Introduction

Tornadoes are among the most violent storms that can occur in the atmospheric boundary layer and are a severe natural hazard. Thousands of tornadoes are reported every year, causing incredible amounts of damage and numerous fatalities. Therefore, it is important to consider tornado-induced wind loads and tornado-borne debris for wind-resistant structural designs. Moreover, detailed information regarding the three-dimensional flow fields of tornadoes is necessary. Many researchers are motivated to observe the dynamics of tornadoes and collect data from full-scale tornadoes using velocity instrumentation. However, due to the unpredictability of tornado paths, collecting data relevant to the internal flow of tornadoes remains challenging. Therefore, experimentally or numerically reproducing tornadoes is an alternative.

Laboratory simulations have provided a reproducible and controllable approach for tornado-related research. Among the experimental studies, Ward (1972) first developed a laboratory simulator with a fan at the top to generate updraft flow and guide-vanes at the floor to provide angular momentum. This approach succeeded in reproducing the evolution of a single-celled vortex into a two-celled vortex, which is a common feature in the most intense tornadoes. Wan and Chang (1972) replaced the guide-vanes with a rotating screen and measured the radial, tangential and vertical velocities with a three-dimensional velocity probe, providing a feasible supplement to field measurements of natural tornadoes. Church et al. (1979) performed a laboratory investigation to clarify the characteristics of tornado-like vortices as a function of the swirl ratio and mapped the transition points at which the flow converts from a single to a double helical vortex configuration and from a double to a triple pattern as a function of the swirl ratio and the Reynolds number. Baker (1981) measured the velocity component and turbulence intensity in the lower portion by employing hot-film anemometry to examine the complicated nature of the flow in the boundary layer of laboratory vortices. Mitsuta and Monji (1984) modified the simulator to induce circulation using four small fans installed in the circulation chamber. The transition of a vortex from a one-celled to a two-celled structure occurred throughout the entire convergence layer in their simulator. The maximum horizontal velocity appeared close to the ground surface; moreover, the height of the maximum velocity was found to be insensitive to the swirl ratio. Monji (1985) investigated the structure of multiple vortices using a guide vane simulator. It was found that the structure of the subsidiary vortex varies with height and that the translational velocity of the subsidiary vortex is sligless than the mean tangential velocity of the parent vortex at high levels.

Most recently, Haan et al. (2008) developed a large laboratory simulator with guide-vanes at the top to make the translation of

* Corresponding author.
E-mail addresses: liuzhenqing1984@hotmail.com (Z. Liu), ishihara@bridge.t.u-tokyo.ac.jp (T. Ishihara).

http://dx.doi.org/10.1016/j.jweia.2015.05.008
0167-6105/

the tornadoes reproducible. In their study, the measurements of the flow structure in the vortex were validated by comparing with mobile Doppler radar observations collected for two major full-scale tornadoes. Matsui and Tamura (2009) conducted velocity measurements with Laser Doppler Velocimetry (LDV) for a tornado-like vortex generated by a Ward-type simulator; the effects of floor roughness were also studied. Using the Particle Image Velocimetry (PIV) method, Tari et al. (2010) quantified both the mean and turbulent flow fields for a range of swirl ratios spanning from Fujita scale 0 to Fujita scale 2, where the Fujita scale is a scale for rating tornado intensity, and suggested that the swirl ratio plays a dominant role in the dynamics of the flow. They also showed that there exists a critical swirl ratio at which the turbulent vortex touches down and the turbulent production approaches maximum values. In addition, they argued that the turbulent flow rather than the mean flow is responsible for the damage associated with tornado events close to the ground. However, in view of the limitations of the observation methods and the extremely complicated flow fields near the ground, it is difficult to collect detailed three-dimensional measurements in the boundary layer, which is thought to be the most important region in tornado-like vortices. Moreover, among all of the laboratory simulators, the definition of the swirl ratio varies from one to another.

With the advancement in computer technology, many numerical studies have been conducted, see Rotunno (1977), Wilson and Rotunno (1986), Nolan and Farrell, (1999), Lewellen et al. (1997), Lewellen et al. (2000), Lewellen and Lewellen (2007), Hangan and Kim (2008), Ishihara et al. (2011), and Ishihara and Liu (2014) for examples. Based on these works, three major approaches can be classified.

The first approach is to solve the axisymmetric Navier–Stokes equations in a two-dimensional cylindrical coordinate system. Rotunno (1977) reported the first numerical study of a tornado vortex and verified the numerical model by comparing with Ward's (1972) laboratory measurements. Wilson and Rotunno (1986) examined a laminar end-wall vortex using the same numerical method. It was found that the dynamics in the boundary layer and core regions are primarily inviscid for the laminar end-wall vortex, and the inviscid nature was demonstrated by examining the balance of terms in the momentum equations. Nolan and Farrell (1999) explored the structure and dynamics of axisymmetric tornado-like vortices. The internal swirl ratio and the vortex Reynolds number were defined; the authors also proposed that the vortex Reynolds number is an effective parameter for predicting the structure of the vortex. However, when the vortex experiences a "breakdown", there will be a sudden expansion and a tendency toward wandering. Therefore, the flow will no longer be axisymmetric, which means it cannot be simulated with a two-dimensional axisymmetric model.

The second approach is to perform three-dimensional full-scale simulations. Lewellen et al. (1997) performed a large-eddy simulation of the interaction of a tornado vortex with the surface in an attempt to answer the questions about the characteristics of turbulent transport in the corner region. It was found that the maximum tangential velocity occurs in the surface layer and is 60% greater than the maximum tangential velocity in the quasi-cylindrical region. Lewellen et al. (2000) explored some of the range of tornado structures that are expected to occur in nature. They defined a local corner swirl ratio and proposed the existence of a critical swirl ratio, which corresponds with the largest tangential velocity very close to the ground. The near-surface intensification was then analyzed in detail and the role of the local corner swirl ratio in determining core flow structure in the tornados was illustrated by Lewellen and Lewellen (2007). However, a comparison with observation data was limited in this study.

The third approach is three-dimensional laboratory-scale simulations. Kuai et al. (2008) simulated the flow field of full-scale and laboratory-simulated tornados and verified that ability of a CFD model to capture the flow characteristics of both tornadoes. They also examined the sensitivity of the simulations to various parameters that might affect the laboratory-simulated tornado. Hangan and Kim (2008) applied an URANS (Unsteady Reynolds-Averaged Navier–Stokes) model to examine the swirl ratio effects on tornado vortices and showed that the high swirl ratio results corresponded with the full-scale data from the Spencer tornado observed by Alexander and Wurman (2005). Ishihara et al. (2011) used an LES turbulent model to simulate the flow fields of two types of tornado vortices and validated the model by comparing with laboratory simulators. The formation of one-celled and two-celled vortices was investigated by examining the axisymmetrically and time averaged results. Ishihara and Liu (2014) focused on a critical state, which is known as vortex touch-down, to understand the dynamics of tornado-like vortices in the boundary layer and corner region. A comprehensive description of the turbulent flow fields was provided; moreover, the turbulent contribution to the mean flow was examined via a force balance analysis. However, the method for scaling the simulations to the real scale must still be clarified.

In this study, a numerical model representing the Ward-type tornado simulator is constructed; four typical tornado vortices are examined using LES. The details of the model are introduced in Section 2 to describe the dimensions, grid distribution and boundary conditions. In Section 3, detailed information regarding the three-dimensional turbulent flow fields of vortices is provided; the force balance in the corner region is also analyzed. The similarity between the simulated tornado-like vortices and the full-scale tornados is investigated and discussed in Section 4.

2. Numerical model and boundary conditions

The governing equations and configurations for the numerical tornado simulator are introduced in Section 2.1 and Section 2.2. The most important parameter determining the structure of tornadoes is the swirl ratio; various definitions have been provided. In Section 2.3, a summary of these definitions is given. Section 2.4 provides an overview of the different case parameters that are considered.

2.1. Governing equations

Momentum and mass are primarily transported by large eddies; therefore, large-eddy simulation (LES) is adopted to simulate tornado-like vortices. In such simulations, large eddies are directly computed, while the influence of eddies smaller than grid spacing are parameterized. The Boussinesq hypothesis is employed, and the standard Smagorinsky–Lilly model is used to calculate the subgrid-scale (SGS) stresses.

The governing equations are obtained by filtering the time-dependent Navier–Stokes equations in Cartesian coordinates (x, y, z), which can be expressed as follows:

$$\frac{\partial \rho \tilde{u}_i}{\partial x_i} = 0 \tag{1}$$

$$\frac{\partial \rho \tilde{u}_i}{\partial t} + \frac{\partial \rho \tilde{u}_i \tilde{u}_j}{\partial x_j} = \frac{\partial}{\partial x_j}\left(\mu \frac{\partial \tilde{u}_i}{\partial x_j}\right) - \frac{\partial \tilde{p}}{\partial x_i} - \frac{\partial \tau_{ij}}{\partial x_j} \tag{2}$$

where $\tilde{u}_i$ and $\tilde{p}$ are the filtered velocities and pressure, respectively, μ is the viscosity, ρ is the density, τ_{ij} is the SGS stress, which is modeled as follows:

$$\tau_{ij} = -2\mu_t \tilde{S}_{ij} + \frac{1}{3}\tau_{kk}\delta_{ij},\ \tilde{S}_{ij} = \frac{1}{2}\left(\frac{\partial \tilde{u}_i}{\partial x_j} + \frac{\partial \tilde{u}_j}{\partial x_i}\right) \tag{3}$$

where μ_t denotes the SGS turbulent viscosity, $\tilde{S}_{ij}$ is the rate-of-strain tensor for the resolved scale, and δ_{ij} is the Kronecker delta. The Smagorinsky–Lilly model is used for the SGS turbulent viscosity:

$$\mu_t = \rho L_s^2 \left|\tilde{S}\right| = \rho L_s \sqrt{2\tilde{S}_{ij}\tilde{S}_{ij}},\ L_s = \min(\kappa d, C_s V^{1/3}) \tag{4}$$

in which L_s denotes the mixing length for subgrid-scales, κ is the von Kármán constant, i.e., 0.42, d is the distance to the closest wall and V is the volume of a computational cell. In this study, C_s is Smagorinsky constant, which is determined to be 0.032 based on Oka and Ishihara (2009).

2.2. Configurations of the numerical tornado simulator

2.2.1. Computational domain and mesh

A Ward-type simulator, which is geometrically same as the study by Matsui and Tamura (2009) except the guide vans are removed in the present study, is chosen; the configurations of the numerical model are shown in Fig. 1. The two most important geometrical parameters are the height of the inlet layer, h, and the radius of the updraft hole, r_0, which are set to 200 mm and 150 mm, respectively. The dominant parameter determining the structure of the tornado vortex is identified as the *swirl ratio*, which is discussed in Section 2.3. The flow rate is calculated by $Q = \pi r_i^2 W_0$, where r_i is the radius of the exhaust outlet and W_0 is the velocity at the outlet. The Reynolds number is expressed as $Re = 2r_0 W_0/\upsilon$. Table 1 summarizes the parameters used in this study.

Considering the axisymmetrical nature of tornado-like vortices, an axisymmetric grid is adopted (see Fig. 2). With the intent to quantitatively investigate the turbulent features in the vicinity of the center and the region near the ground, a fine mesh is considered in the convergence region, in which 86 nodes in the radial direction and 45 nodes in the vertical direction are used; the minimum size of the mesh is approximately 1 mm in the radial direction and 0.1 mm in the vertical direction. The spacing ratios in the two directions are less than 1.2 to avoid a sudden change in the grid size. The total number of grid points is approximately 7.8×10^5. We have compared the simulated flow field with that by Ishihara and Liu (2014) in which the grid is coarser than the present study. The numerical results in the two simulations have shown good agreements with experiment by Matsui and Tamura (2009), indicating that the results are grid independent.

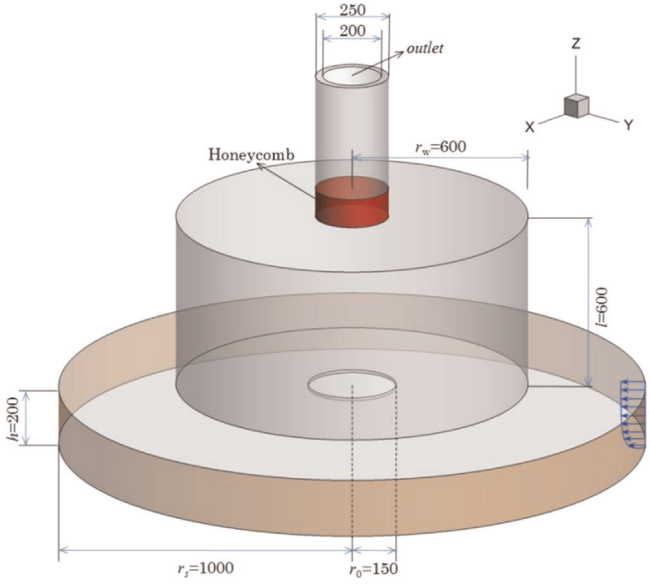

Fig. 1. The geometry of the model (mm).

2.2.2. Boundary conditions

When the wall-adjacent cells are in the laminar sublayer, the wall shear stresses are obtained from the laminar stress–strain relationship:

$$\frac{\tilde{u}}{u_\tau} = \frac{\rho u_\tau y}{\mu} \tag{5}$$

If the mesh cannot resolve the laminar sublayer, it is assumed that the centroid of the wall-adjacent cells falls within the logarithmic region of the boundary layer, and the law-of-the-wall is employed as follows:

$$\frac{\tilde{u}}{u_\tau} = \frac{1}{\kappa}\ln E\left(\frac{\rho u_\tau y}{\mu}\right) \tag{6}$$

where $\tilde{u}$ is the filtered velocity tangential to wall, y is the distance between the center of the cell and the wall, u_τ is the friction velocity, and the constant E is 9.793. In tornado-like vortices, a flow with both axial and radial pressure gradients is present; however, the radial pressure gradient dominates the axial pressure gradient in the near-surface region, which implies the wall function can be used. In most of the region, the wall-adjacent cells are in the laminar sublayer. The maximum of $y+$ is 10 in the core region of the vortex.

The velocity profiles at the inlet are specified as follows:

$$\begin{cases} U_{rs} = U_1\left(\dfrac{z}{z_1}\right)^{1/n} \\ V_{rs} = -U_{rs}\tan(\theta) \end{cases} \tag{7}$$

where U_{rs} and V_{rs} are radial velocities and the tangential velocities at $r = r_s$ (see Fig. 1), n is equal to 7, the reference velocity U_1 and the reference height z_1 are set to 0.24 m/s and 0.01 m, respectively, by matching the velocity profile at the inner ring of the guide vanes in Ishihara et al. (2011), and θ is the inflow angle. In Eq. (7), U_1 is a constant; moreover, U_{rs} is a function of z. The inflow angle θ is adjusted to change the swirl ratio. Porous media is applied to model a honeycomb in which no drag force is added in the vertical momentum equation but almost infinite drag forces are added in the horizontal directions. Therefore, the fluid can move freely in vertical direction with nearly no motion in the horizontal directions, which is similar to fluid in a honeycomb. At the outlet, the outflow boundary condition is used, which means that the gradients in pressure and velocities are set to zero here.

2.2.3. Solution scheme and solution procedure

The finite volume method is used for the simulations. The second-order central difference scheme is used for the convective and viscous terms, and the second-order implicit scheme is employed for the unsteady term. The SIMPLE (semi-implicit pressure linked equations) algorithm is used to solve the discretized equations, which was shown by Ferziger and Peric (2002).

The initial transient effects were found to disappear after 10 s; therefore, the data for time sampling begin at 10 s and then the flow fields are averaged temporally from 10 s to 30 s. A stationary condition for time sampling can be achieved by evaluating relative errors in the maximum mean tangential velocity within the cyclostrophic balance region, V_c, which becomes less than 1% when the data from 10 s to 30 s are used. The time sampling error is calculated by finding the difference of the time averaged result

Table 1
The parameters used in this study.

Height of the inlet layer: h	200 mm	Reynolds number: $Re=2r_0W_0/\upsilon$	1.60×10^5
Radius of the updraft hole: r_0	150 mm	Non-dimensional time step: $\Delta tW_0/2r_0$	0.032
Internal aspect ratio: $a=h/r_0$	1.33	Mesh size in the radial direction	1.0–25.0 mm
Radius of the exhaust outlet: r_t	200 mm	Mesh size in the vertical direction	0.1–5.0 mm
Radius of the convergence region: r_s	1000 mm	Mesh number	784,200
Velocity at the outlet: W_0	9.55 m/s		
Total outflow rate: $Q=\pi r_t^2W_0$	0.3 m^3/s		

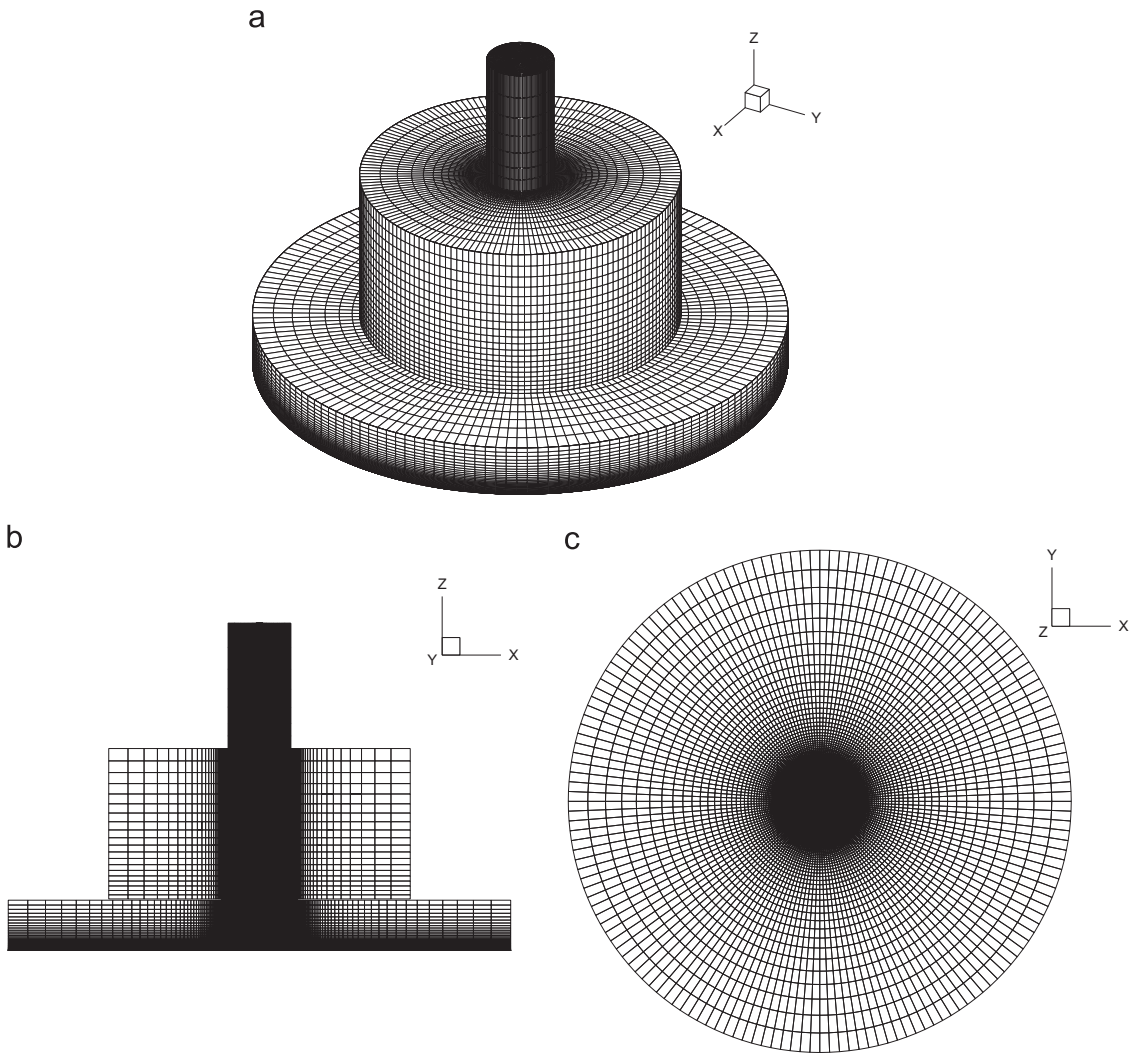

Fig. 2. Mesh of the numerical model: (a) isometric view, (b) lateral view, and (c) bird's-eye view.

Table 2
Case settings and the accompanying tornado vortex parameters.

Case name	Inflow angle (deg)	S_E	S	S_c	V_c (m/s)	r_c (m)	r_2 (m)	z_2 (m)
Case1	46.8	0.4	0.02	0.71	10.7	0.014	0.123	0.049
Case2	58.0	0.6	0.06	1.59	9.8	0.024	0.120	0.039
Case3	64.9	0.8	0.12	2.36	9.1	0.035	0.146	0.039
Case4	69.4	1.0	0.23	2.93	9.6	0.047	0.150	0.042
Case5	76.0	1.5	0.34	4.16	11.0	0.054	0.152	0.041
Case6	79.4	2.0	0.69	5.39	12.4	0.073	0.171	0.039
Case7	82.1	2.7	1.06	6.74	14.3	0.084	0.193	0.036
Case8	83.5	3.3	1.58	7.96	16.0	0.097	0.239	0.035
Case9	84.4	3.8	2.44	8.89	18.6	0.112	0.295	0.034

of V_c from 10 s to 10 s+T/2 and that from 10 s+T/2 to 10 s+T, where T is the time used for time sampling. The cyclostrophic balance region is the height at which the centrifugal force balances the pressure gradient force. In this study, this region is located at a height of $z=r_0$.

2.3. Definitions of the swirl ratio

For the laboratory simulators used by Church et al. (1979), Monji (1985), Mishra et al. (2008), Matsui and Tamura (2009) and Tari et al. (2010) and the numerical simulators used by Rotunno (1977), Wilson and Rotunno (1986), and Ishihara et al. (2011), the swirl ratio has historically been defined as the ratio of the angular

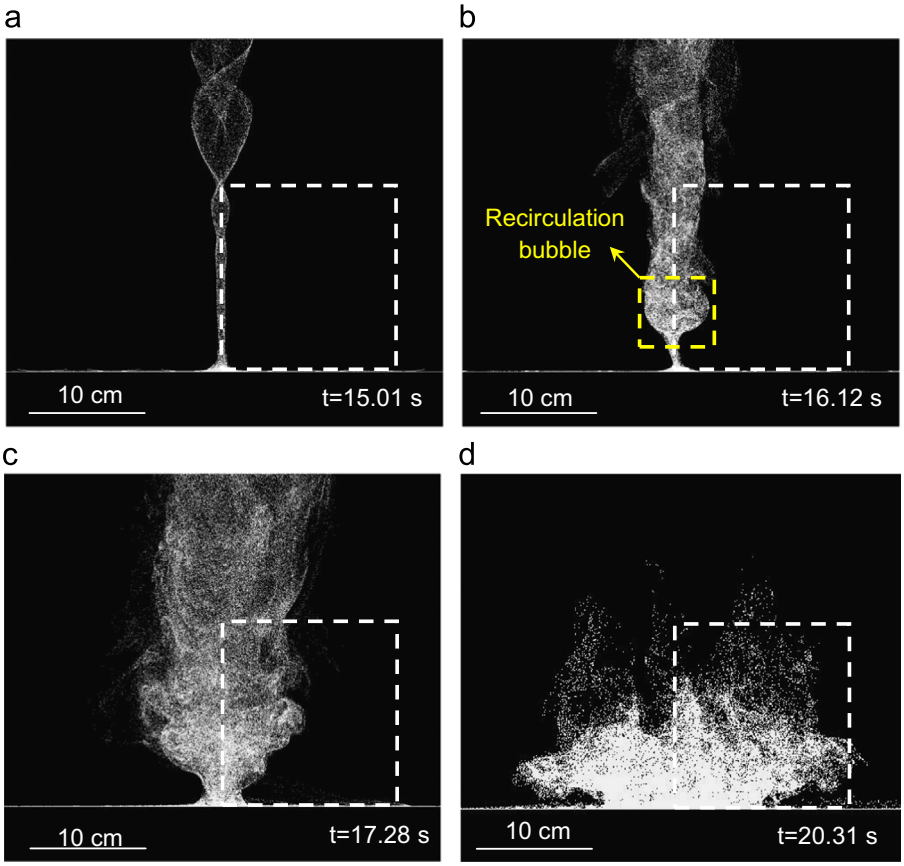

Fig. 3. Flow visualization by injecting tracer particles from the ground for four typical tornado vortex types: (a) single vortex, S=0.02, (b) vortex breakdown, S=0.06, (c) vortex touch-down, S=0.23, and (d) multi-vortex, S=2.44. White dashed rectangulars indicate the regions considered when plotting the streamlines shown in Fig. 4. A yellow dashed square in Fig. 3(b) shows the region of a recirculation bubble. (For interpretation of the references to color in this figure legend, the reader is referred to the web version of this article.)

momentum to the radial momentum in the vortex, which can be expressed as follows:

$$S_E = \frac{\Gamma_\infty}{2Qa} = \frac{\tan\theta}{2a} \tag{8}$$

where Γ_∞ is the free-stream circulation at the outer edge of the convergence region, $\Gamma_\infty = 2\pi r_s h V_{rs}$, r_c is the location at which V_c occurs, and a is the aspect ratio, $a = h/r_0$. Moreover, h and r_0 are the height of the inlet layer and the radius of the updraft hole, respectively, and Q is the volume flow rate. When a circulation is imposed by guide vanes, the ratio of the free-stream circulation to the volume flow rate can easily be replaced by $\tan\theta$, where θ is the angle of the guide vanes. All of the parameters in the above-proposed swirl ratio are either under the control of the modelers or explicitly determined by the domain geometry; thus, this definition can be classified as an external swirl ratio.

However, the representative vortex structures did not occur at the same swirl ratios when the experiments were conducted by some simulators with the guide vanes located at the top, which was shown by Haan et al. (2008). In those cases, the swirl ratio was modified as follows:

$$S = \frac{r_c \Gamma_c}{2Qh} = \frac{\pi r_c^2 V_c}{Q} \tag{9}$$

in which the circulation in the core region of the vortex is $\Gamma_c = 2\pi r_c h V_c$. In this expression, the parameters are no longer explicit because V_c and r_c are obtained based on the flow field measurements and only the flow rate can be decided beforehand. This definition can be classified as a mixed swirl ratio. In Section 3, the mixed swirl ratio S will be applied to perform a systematic comparison of the flow fields.

For full-scale tornado's occurring in nature, the external and the mixed swirl ratios are not applicable because the circulation and the flow rate are not controllable. Thus, an internal swirl ratio, S_I, is defined based on the measured rotation and flow rate in a control volume surrounding the vortex, which can be expressed as follows:

$$S_I = \frac{r_v}{2h_v} = \frac{\int_0^{h_v} \Gamma(r_v, z)dz}{\int_0^{r_v} W(r, h_v)2\pi r dr} \tag{10}$$

where r_v and h_v are the radius and height of the control volume surrounding the vortex, while $\Gamma = 2\pi V r$ is the circulation per unit height. Haan el al. (2008) examined the internal swirl ratio and found that this internal swirl ratio has the same descriptive characteristics as the external and mixed swirl ratios. However, the internal swirl ratio depends on the chosen dimensions of the control volume and is found to have higher values for larger control volumes and lower values for smaller ones.

Lewellen et al. (2000) proposed a local corner flow swirl ratio, S_c, which is expressed as follows:

$$S_c = \frac{r_c^* \Gamma_\infty^{*2}}{\Upsilon} \tag{11}$$

where r_c^* is the characteristic length scale that is defined as $r_c^* \equiv \Gamma_\infty^*/V_c$. The circulation per unit height in the outer region is expressed as $\Gamma_\infty^* = V(r_2, z_2)r_2$, and the total depleted circulation flux flowing through the corner flow region, Υ, is expressed as follows:

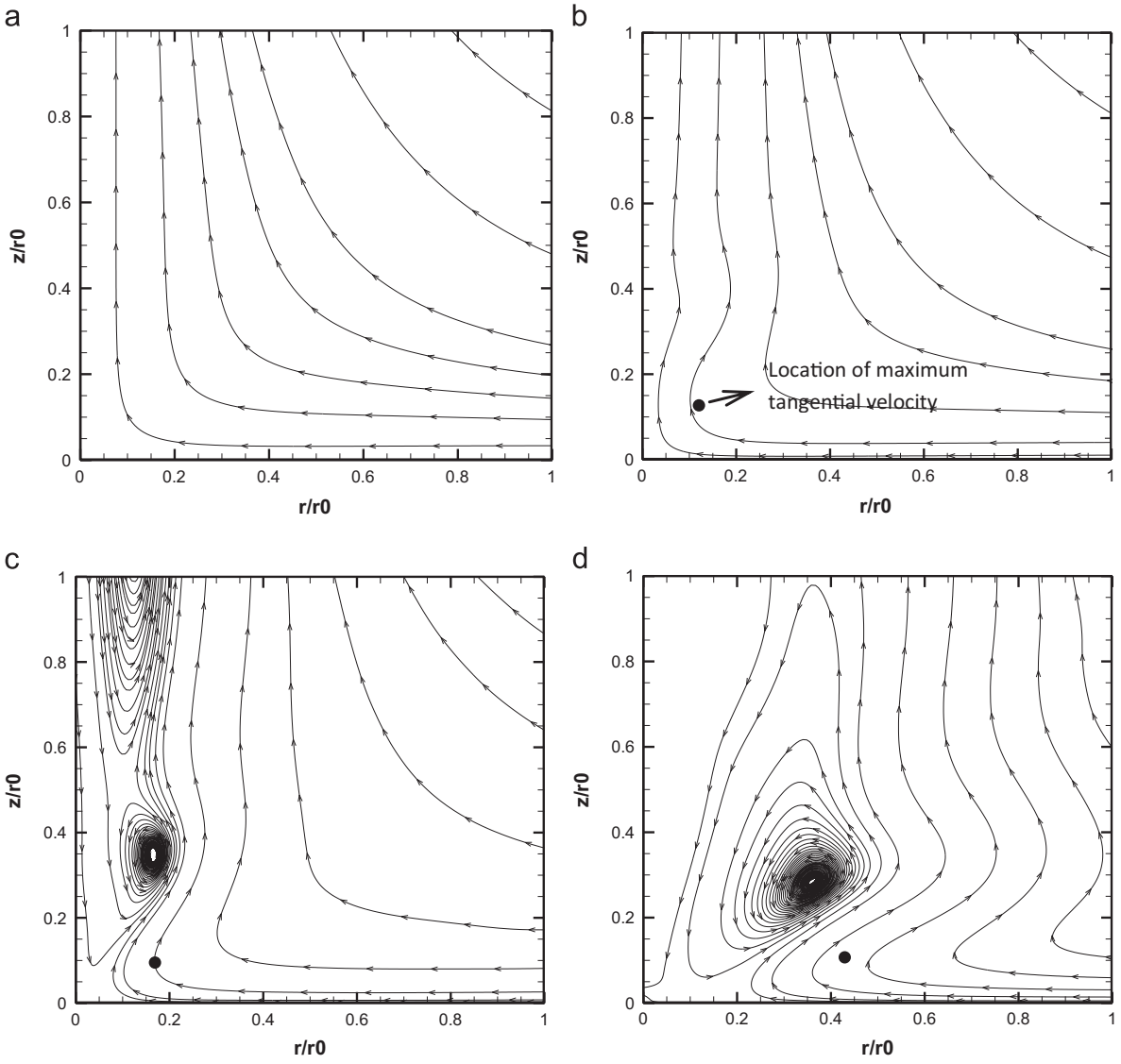

Fig. 4. Streamlines of the averaged flow fields in the radial-vertical plane ($1r_0 \times 1r_0$) for four typical tornado-like vortices: (a) weak vortex, $\underline{S}$=0.02, (b) vortex breakdown, S=0.06, (c) vortex touch-down, S=0.23, and (d) multi-vortex, S=2.44. The maximum azimuthal velocity is marked as "•".

$$\Upsilon \approx 2\pi \int_0^{r2} W(r, z_2)\Gamma_d(r, z_2) r dr \tag{12}$$

where Γ_d is the depleted angular momentum, which is defined as $\Gamma_d(r, z_2) = V(r_2, z_2)r_2 - V(r, z_2)r$, and r_2 and z_2 are determined following Lewellen et al. (2000) and are shown in Table 2 for each case in this study. In Section 4, the local corner swirl ratio, S_c, is used for the similarity analysis.

2.4. Overview of the different case parameters

The case settings and parameters are shown in Table 2. In this study, 9 cases are considered, in which Case1, Case2, Case4 and Case9, corresponding to single-celled vortex, vortex breakdown, vortex touch-down and multi-vortex cases, respectively, are four typical tornado vortices and are used for detailed flow field analysis in the following discussion. The flow pattern from the single-celled vortex to the vortex touch-down is very sensitive to the change of the swirl ratio. Therefore in order to capture the typical types of tornado from the single-celled vortex to the vortex touch-down, the external swirl ratio increases at a small step size of 0.2. After vortex touch-down, the flow pattern becomes similar, therefore larger step sizes are used and when S_E=3.8 the flow fields become comparable with the Spencer tornado as shown in the following discussion.

3. Flow fields characteristics

In this section, the flow fields are first visualized in Section 3.1 to provide a general image of tornado structures under different swirl ratios. Then, the mean and turbulent flow fields are examined in detail in Section 3.2 and Section 3.3, respectively. Finally, the force balances in the radial and vertical directions are investigated in Section 3.4.

3.1. Flow patterns

To make the air flow visible, tracer particles are injected from the bottom of the model. The diameter of the tracer particles is uniform and equal to 1×10^{-5} m; the injection rate is 0.1 g/s. The gravity of the particles is neglected and their positions are directly integrated without considering their interaction with the flow. The particles are not released until the flow fields are in the quasi-

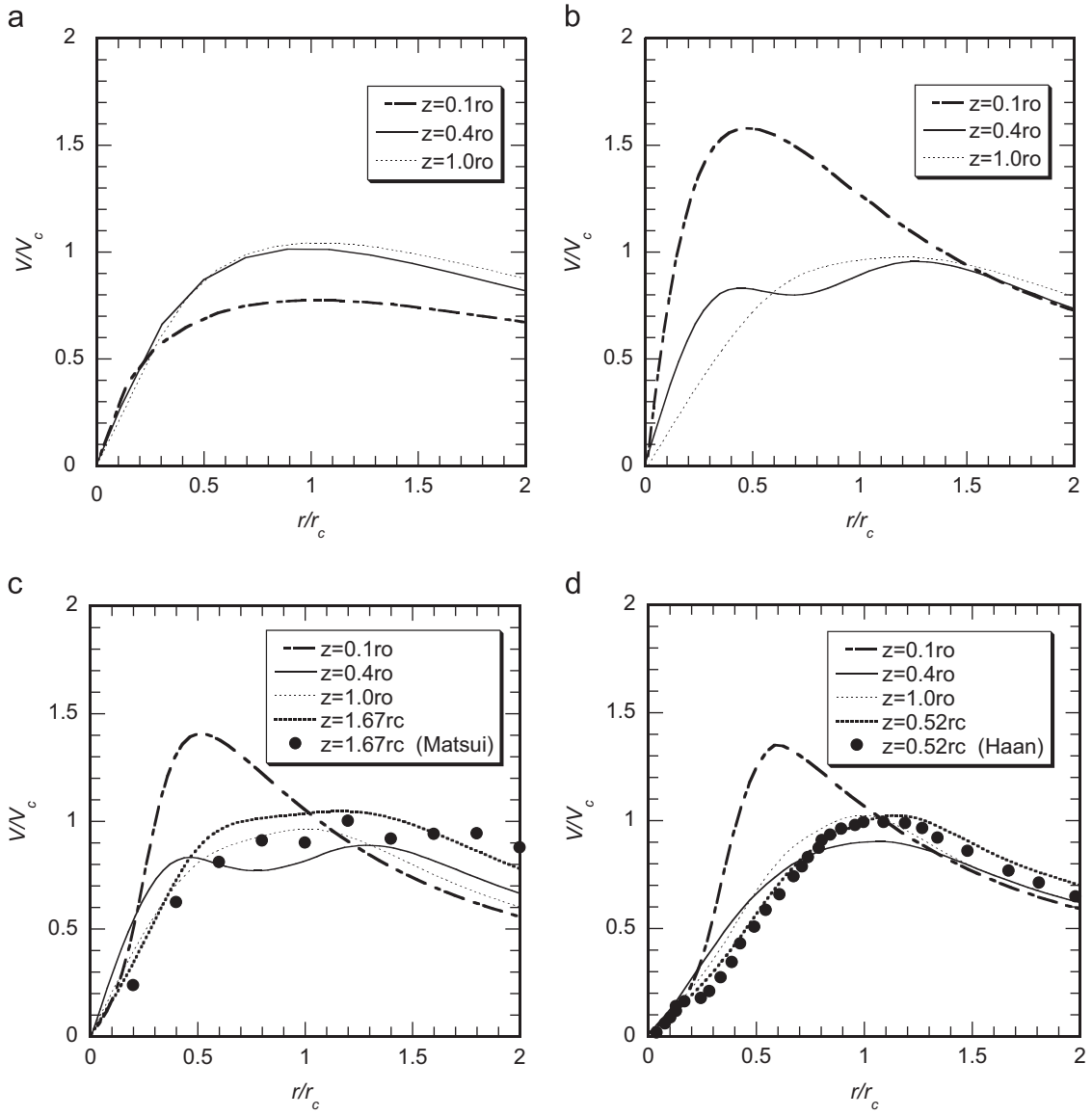

Fig. 5. Radial profiles of the normalized tangential velocity for four typical tornado-like vortices: (a) weak vortex, $S=0.02$, (b) vortex breakdown, $S=0.06$, (c) vortex touch-down, $S=0.23$, and (d) multi-vortex, $S=2.44$.

steady stage to eliminate the effect of initial transients in the solution.

As the swirl ratio is increased, the vortex goes through various stages (Fig. 3). In Fig. 3, the white dashed rectangular regions indicate the regions considered when plotting the streamlines shown in Fig. 4. For the case of $S=0.02$, it is found that the central core is smooth and laminar. The core extends upward from the surface to higher levels and spreads slightly, which is shown in Fig. 3(a). The water vapor forms a spiral surface at high elevations, which was also captured by Ward (1972). For a larger value, $S=0.06$, a vortex breakdown occurs in which the flow transitions from a tight, laminar vortex to a broader, turbulent state. The laminar flow with a very narrow core in the lower portion moves upward until it suddenly expands into a recirculation bubble, which is shown by a yellow dashed square in Fig. 3(b). In the transition region, the flow is typically turbulent. The water vapor shows that the breakdown is unstable and oscillates about a mean position. The radius of the vortex core increases and the altitude of the breakdown decreases as the swirl ratio increases. In Fig. 3(c), at $S=0.23$, the vortex breakdown occurs slightly above the boundary layer. In the lower portion, the radial jet and the downward jet break away from the vertical axis and generate a stretched bubble at the interface between the near-surface conical vortex and the aloft cylindrical vortex. This state has been termed as vortex touch-down and was examined in detail by Ishihara and Liu (2014). A further increase in the swirl ratio results in the breakdown being forced further toward the surface layer. The core of the vortex expands substantially and leaves a relatively calm inner sub-core, which is shown in Fig. 3(d) for $S=2.44$. Concurrent with the expansion of the core, the inner downdraft penetrates to the ground surface; a family of several secondary vortices rotating around the main vortex is evident.

Church et al. (1979) and Monji (1985) reported the vortex type as a function of the Reynolds number and the swirl ratio. It was concluded that the vortex type depends slightly on the Reynolds number; this dependency decreases for higher Reynolds numbers. In this study, it is assumed that the structures of the vortices depend primarily on the swirl ratio.

The predicted streamlines of the averaged flow fields in the radial-vertical plane are shown in Fig. 4; the x and z axes are normalized using r_0. The arrows represent the direction of the wind. The location of the maximum tangential velocity is marked

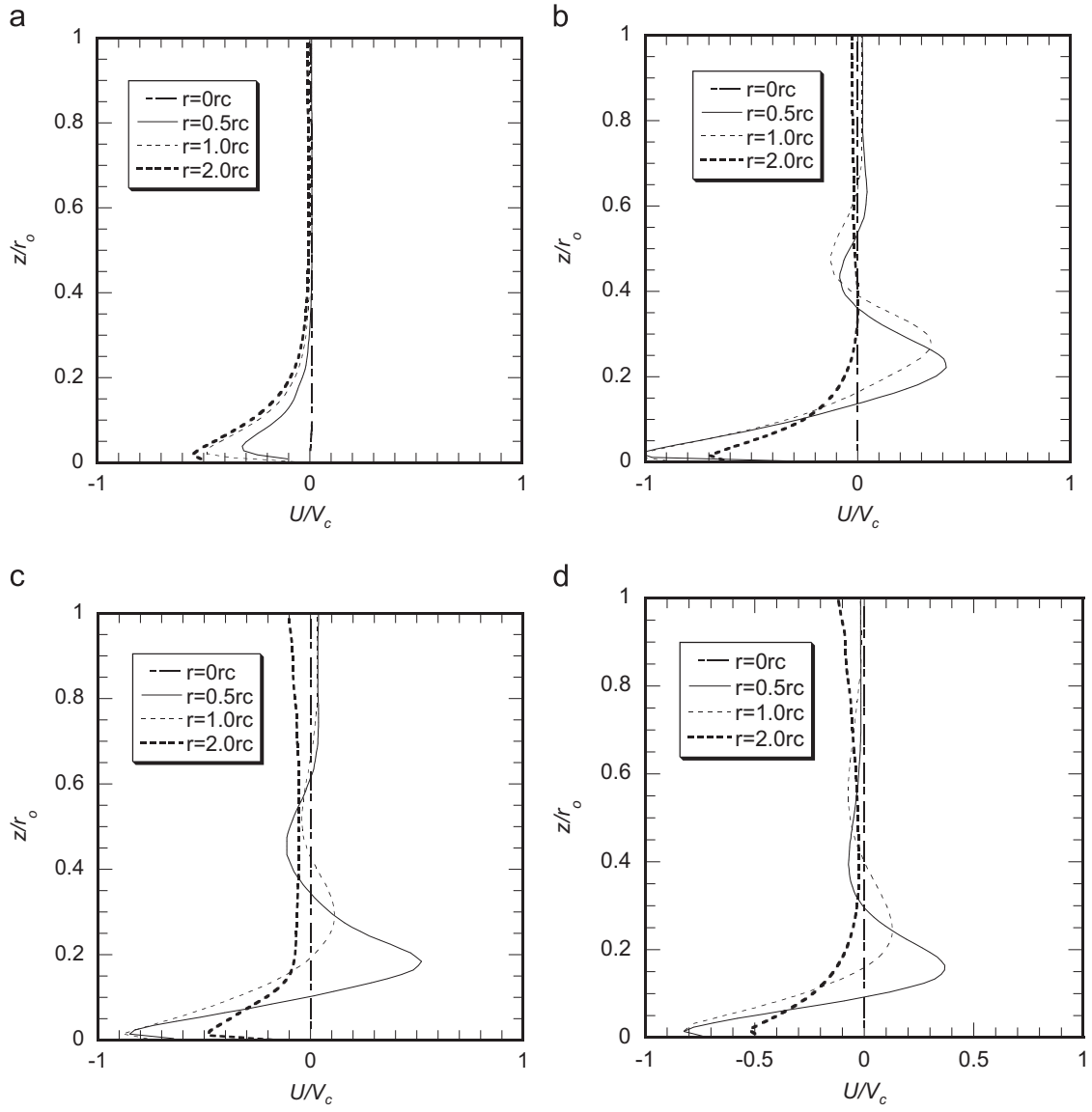

Fig. 6. Vertical profiles of the normalized radial velocity for four typical tornado-like vortices: (a) weak vortex, $S=0.02$, (b) vortex breakdown, $S=0.06$, (c) vortex touch-down, $S=0.23$, and (d) multi-vortex, $S=2.44$. Positive direction of the radial velocity is outward the center.

as "•". The calculation of the averaged values at each position was performed by averaging the time-averaged values at the same radius and height over twelve azimuthal angles.

For the case of $S=0.02$, the boundary layer inflow penetrates all the way to the axis before turning upward into the strong updraft, forming a single-celled type vortex, which is shown in Fig. 4(a). When increasing the swirl ratio to the vortex breakdown stage, the boundary layer inflow also penetrates to the center and turns upward; however, the vertical flow breaks away from the vertical axis forming an expanded bubble. At the vortex touch-down state, the inner downdraft penetrates to the location just above the surface, while the stretched bubble shifts closer to the surface, which is shown in Fig. 4(c) for $S=0.23$. As the swirl ratio increases to 2.44, which is shown in Fig. 4(d), the radial jet cannot penetrate to the center and instead moves upward and outward within a stagnation ring. This result can be explained as follows: the inner downdraft touches the surface and changes its direction to an outward radial jet, which interacts with the inward radial jet and prevents it from penetrating closer to the axis. Although the radial location of the maximum tangential velocity moves outward when increasing the swirl ratio, only small variations in the height occur.

A quantitative analysis can be performed by examining the distributions of the mean velocity components. In the following discussion, the maximum tangential velocity in the cyclostrophic balance region, V_c, is used to normalize the flow fields. The vertical dimension is scaled by the radius of the updraft hole, r_0. The selection of this non-dimensional method in the vertical direction is based on the consideration that the height of the maximum tangential velocity is nearly constant. Moreover, the radial distance is normalized by the core radius of the tornado vortex in the cyclostrophic balance region, r_c.

3.2. Mean flow fields

The radial profiles of the normalized mean tangential velocity, V/V_c, versus the nondimensional radial distance are shown in Fig. 5 (a). The tangential velocity is the component perpendicular to the plane plotted in Fig. 4. For the very low swirl ratio case, i.e., $S=0.02$, the mean tangential velocity field does not change with height except for the layer very near the ground. The radius of the vortex core, R, which is defined based on the location of the maximum tangential velocity at each elevation, is nearly

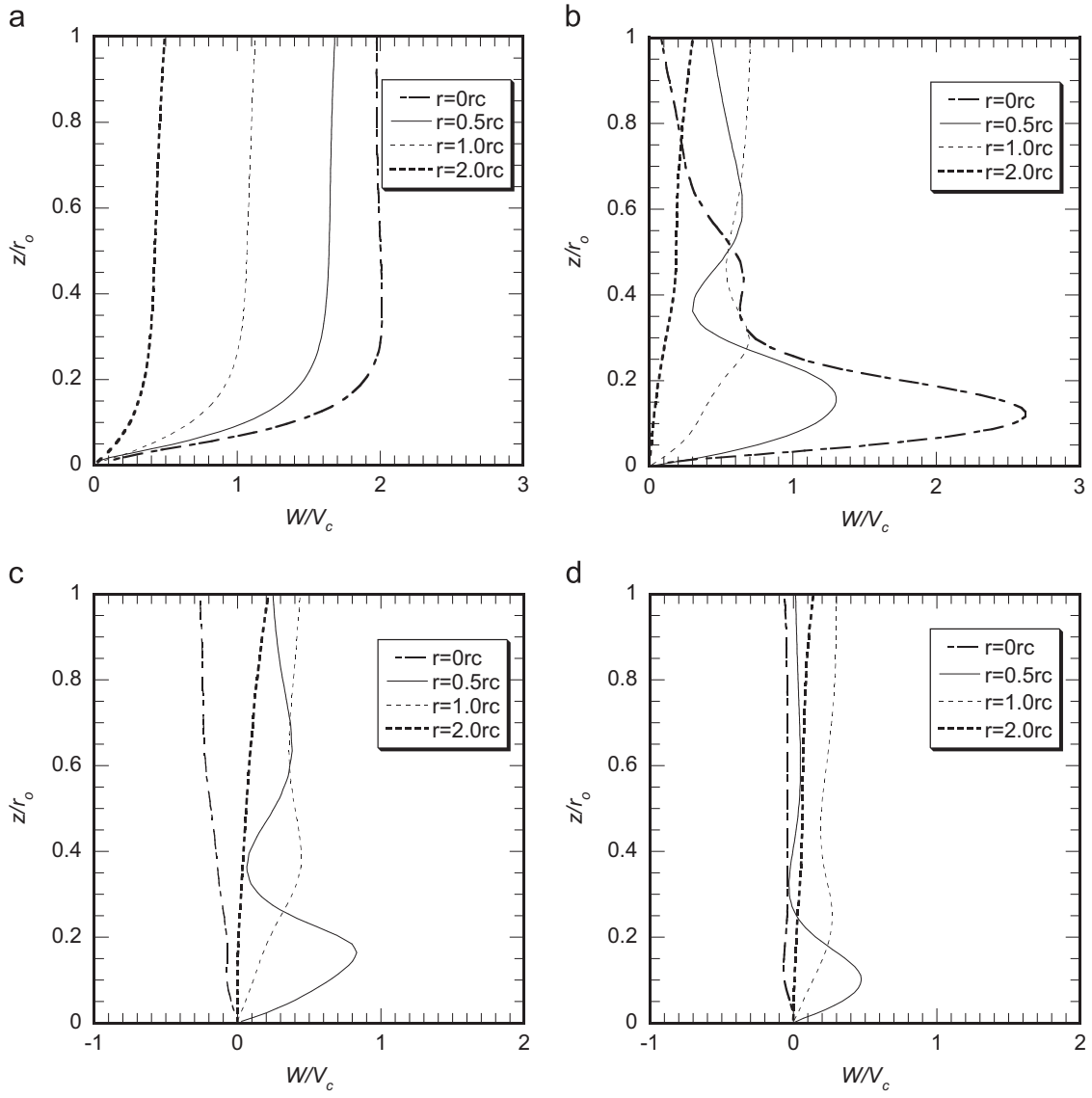

Fig. 7. Vertical profiles of the normalized vertical velocity for four typical tornado-like vortices: (a) weak vortex, $S=0.02$, (b) vortex breakdown, $S=0.06$, (c) vortex touch-down, $S=0.23$, and (d) multi-vortex, $S=2.44$.

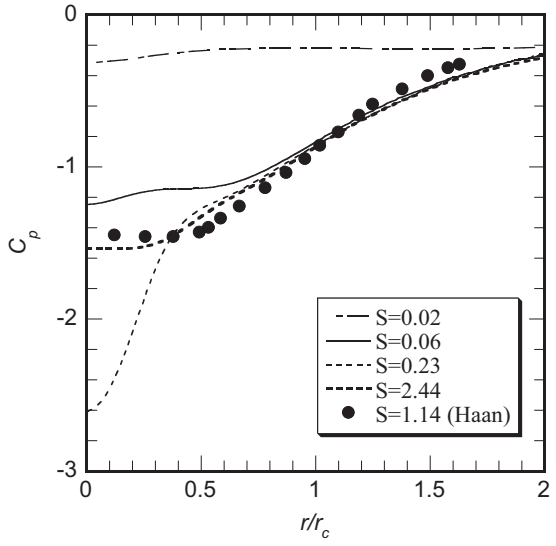

Fig. 8. Radial distribution of the surface pressure coefficient at the surface. V_c is used to normalize P.

consistent. For a larger swirl ratio, i.e., $S=0.06$, three-dimensional characteristics are obvious in Fig. 5(b). Swirl overshooting appears at the surface layer with a maximum tangential velocity of 1.6 times V_c, and the core radius increases from $0.5r_c$ to $1.0r_c$ with height, ultimately forming a funnel shape. By further increasing the swirl ratio to the touch-down and multi-vortex stages, the ratio of the maximum tangential velocity, V_{max}/V_c, is nearly constant at approximately 1.4, and the radial location of V_{max} changes very slightly, with a value of approximately $0.5r_c$. The results of the case with $\theta=60°$ in the study by Matsui and Tamura (2009) and the *Vane5* case, whose mixed swirl ratio S was set to 1.14, in the study by Haan et al. (2008) are also plotted and compared with Case4 and Case9, respectively. It is found that the simulated results in this study agree well with these previous experiments.

Fig. 6 presents the normalized vertical profiles of the mean radial velocity, which is negative toward the core. In the case of $S=0.02$, the radial velocity reaches its maximum magnitude, $0.6V_c$, in the outer region and decreases toward the center, which is shown in Fig. 6(a). With an increase in the swirl ratio, i.e., $S=0.06$, an inversion point emerges in the core, and the peak magnitude of radial velocity reaches approximately $1V_c$ at the ring of the core, $r=1r_c$. By further increasing the swirl ratio to the case of $S=0.23$

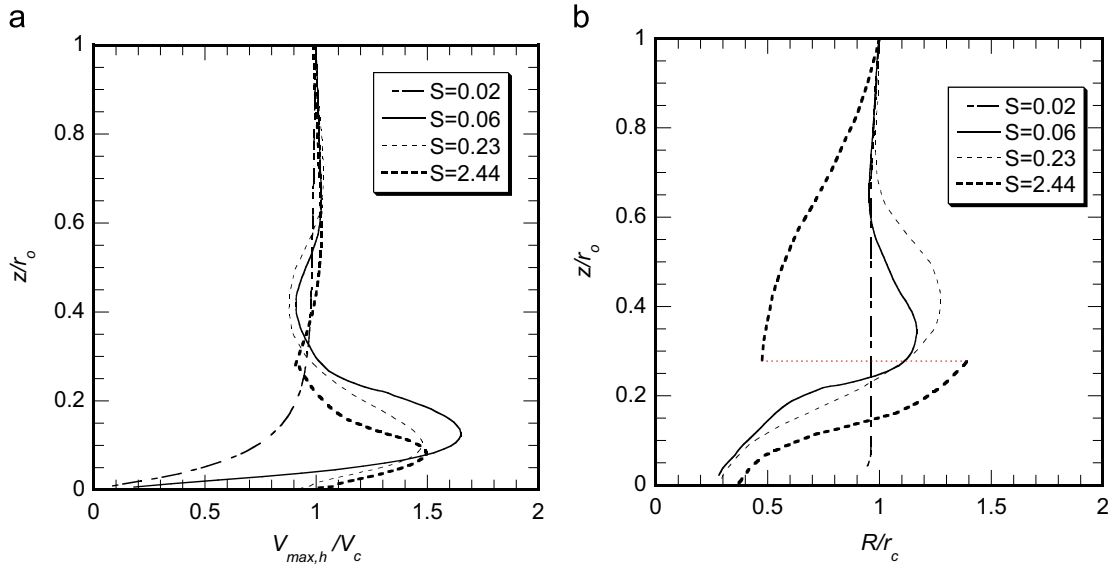

Fig. 9. Vertical distribution of (a) the maximum tangential velocity and (b) the core radius with respect to height.

Table 3
Numerical results for the representative parameters.

Case name	S	U_{min}/V_c	V_{max}/V_c	W_{max}/V_c	$r_{v,max}/r_c$	$h_{v,max}/r_0$	C_{pmin}
Case1	0.02	–	–	–	–	–	−0.245
Case2	0.06	−1.082	1.602	2.582	0.542	0.133	−1.231
Case3	0.12	−0.945	1.341	1.110	0.600	0.107	−2.536
Case4	0.23	−0.958	1.354	0.646	0.574	0.100	−2.601
Case5	0.34	−0.873	1.245	0.545	0.648	0.093	−2.571
Case6	0.69	−0.895	1.379	0.460	0.589	0.087	−2.232
Case7	1.06	−0.825	1.329	0.329	0.655	0.080	−2.050
Case8	1.58	−0.856	1.363	0.294	0.598	0.073	−1.877
Case9	2.44	−0.855	1.430	0.269	0.563	0.067	−1.596

and $S=2.44$, the radial velocity profiles exhibit remarkable similarity with the vortex breakdown case.

The maximum magnitude of the radial velocity reaches approximately $1V_c$, and the thickness of the inversion point decreases as the radial distance decreases. A comparison between the profiles of the different cases shows that a major portion of the radial flow is concentrated in a thin layer near the ground, having a depth less than $0.2r_0$. This concentration of the radial flow is due to the radial pressure gradient.

The difference between the profiles of the mean axial velocity, W, for the four states is well defined, which is shown in Fig. 7. In the case of $S=0.02$, the axial velocity reaches its maximum value at the center and decreases with increasing radius. For the case $S=0.06$, vertical overshooting occurs in the center at low levels; the maximum axial velocity, W_{max}, is approximately 2.6 times V_c. This pronounced vertical overshooting can be attributed to the radial jet changing its direction upward; however, when moving to higher levels, the axial velocity decreases dramatically and ultimately becomes nearly zero at $z=1r_0$. The peak axial velocity decreases with increasing radial distance, while the corresponding height is shifted upward. By further increasing the swirl ratio to the vortex touch-down state, the direction of the axial velocity becomes downward at the center. The maximum axial velocity decreases to $0.8V_c$, and the corresponding location moves to $r=0.5r_c$. Moreover, the axial velocity is concentrated in the region defined by $0.5r_c < r < 1.0r_c$. For a larger swirl ratio, i.e., $S=2.44$, the downward axial velocity becomes weaker than that in the vortex touch-down case, which is related to the fact that the core of the vortex expands and leaves a calm inner sub-core.

The pressure coefficient at the surface, C_p, is another important parameter for wind-resistant designs. In this study, the pressure coefficient is calculated using static pressure at the inlet as a reference pressure and V_c to normalize it. The surface pressure coefficient profiles for various swirl ratios are shown in Fig. 8. In the weak vortex state, the profile is nearly flat and exhibits only a small pressure drop at the center. In the vortex breakdown case, the pressure drop is comparable with that of the multi-vortex case, while in the case of $S=0.23$, a rapid decrease in pressure coefficient at the center, reaching -2.6, can be found, indicating that the vortex bubble moves toward the surface layer. By further increasing the swirl ratio to the multi-vortex state, the profile becomes flat near the center. The flat profile of the surface pressure coefficient in the center was also shown in the *Vane5* case in Haan et al. (2008) and agrees well with the results of Case9 (see Fig. 8). This flat profile is likely due to the central downdraft along the vortex axis, which was discussed by Haan et al. (2008).

Fig. 9 illustrates the vertical distribution of the maximum tangential velocity, $V_{max,h}$, and the core radius, R. It is clear that at high levels, the maximum tangential velocity is approximately $1V_c$ at $r=1r_c$ (see Fig. 9(a)); however, close to the ground, the maximum tangential velocity reaches approximately $1.5V_c$. This increase in the tangential velocity is important for wind-resistant designs because most engineering structures exist in the surface layer. By comparing the maximum tangential velocity profiles, a similarity in the shape is revealed after the vortex breakdown stage. The maximum tangential velocity initially increases to a maximum at a height of $0.1r_0$. For higher levels, the maximum tangential velocity decreases to a small value and becomes constant. The core radius, R, is nearly constant for the weak vortex case, which is shown in Fig. 9(b). As the swirl increases, the core radius increases from a value less than r_c to a maximum of $1.2r_c$ before approaching a constant, r_c at high levels. The distribution of the core radii for the cases of $S=0.06$ and $S=0.23$ are similar. However, by further increasing the swirl ratio, a discontinuity emerges in the profile, which was also captured in the simulations by Hangan and Kim (2008).

Table 3 summarizes the variables used to provide comprehensive information about the surface intensification and the geometry of tornado vortices as a function of the swirl ratio, where U_{min} is the minimum averaged radial velocity, V_{max} is the maximum averaged tangential velocity, W_{max} is the maximum vertical velocity, $r_{v,max}$ and $h_{v,max}$ are the radius and height of the location

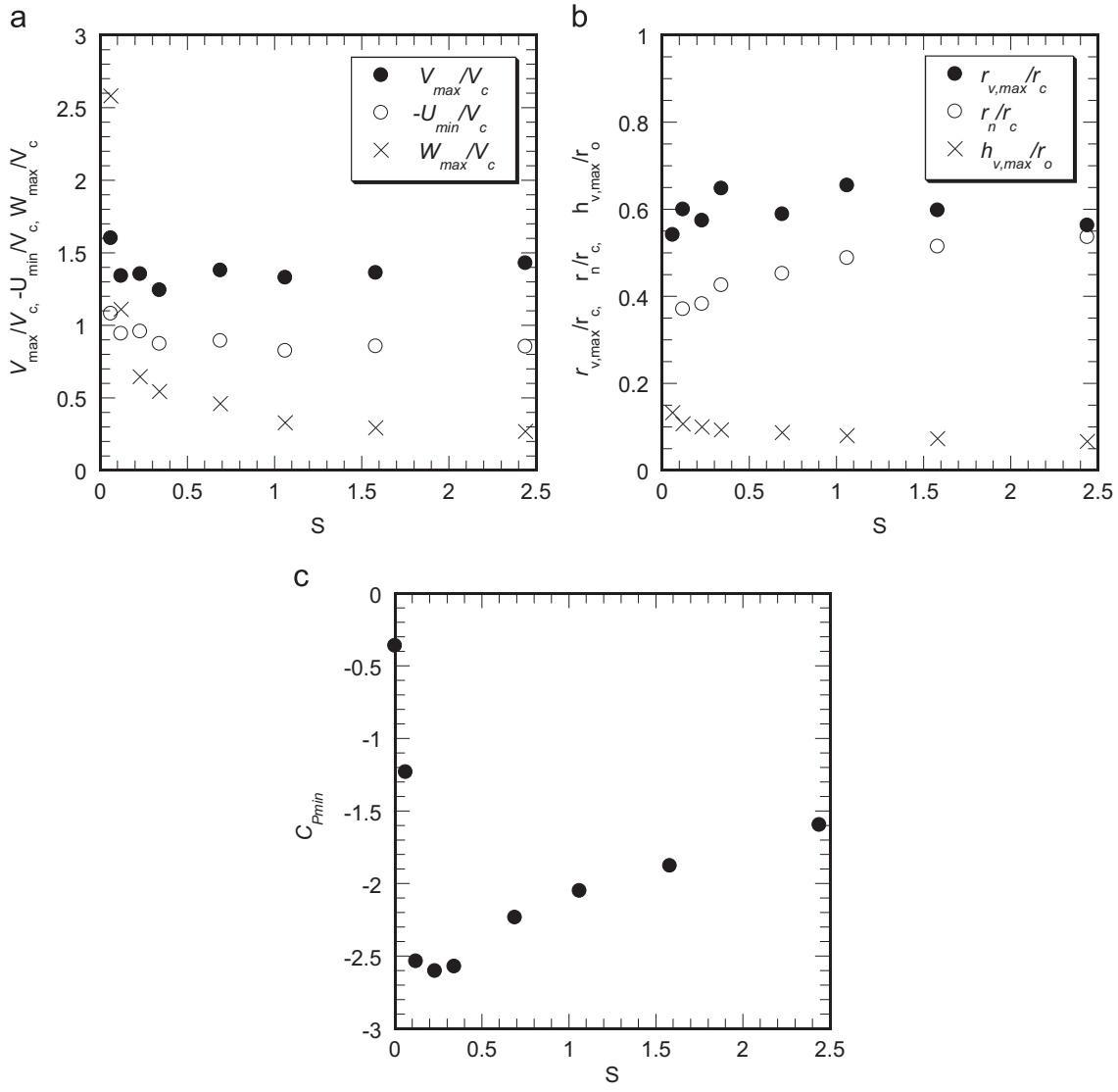

Fig. 10. Representative parameters as a function of the swirl ratio: (a) V_{max}/V_c, $-U_{min}/V_c$, W_{max}/V_c, (b) $r_{v,max}/r_c$, r_n/r_c, $h_{v,max}/r_0$, and (c) C_{pmin}.

of the maximum tangential velocity, respectively, and P_{min} is the minimum pressure at the surface.

The non-dimensional representative velocities, i.e., V_{max}/V_c, $-U_{min}/V_c$, and W_{max}/V_c, are plotted as a function of the mixed swirl ratio in Fig. 10(a). For the weak vortex state, there is no intensification near the ground; therefore, the subsequent examination will only be performed for the stages after the vortex breakdown. In Fig. 10(b), V_{max}/V_c, $-U_{min}/V_c$, and W_{max}/V_c reach maximum values during the vortex breakdown stage. Thereafter, the values of these parameters decrease and reach constant values. The non-dimensional representative geometry parameters, i.e., $r_{v,max}/r_c$ and $h_{v,max}/r_0$, are scattered around 0.6 and 0.08, respectively. As shown in Fig. 10(c), at the vortex touch-down stage, the minimum pressure coefficient at the surface, C_{pmin}, reaches a maximum value due to the vortex bubble extended to the surface layer. After the vortex touch-down stage, the vortex bubble diminishes; thereafter, the inner downward flow touches the ground, which increases C_{pmin}.

3.3. Turbulent flow fields

Through a detailed examination of the turbulent flow fields for tornado-like vortices at touch-down, Ishihara and Liu (2014) indicated that it is not sufficient to characterize only the mean flow fields because the turbulent characteristics close to the ground are also important for tornado-like vortices. Recently, Tari et al. (2010) provided turbulent information for the tornado-like vortices with different swirl ratios based on PIV experiments; however, the turbulent information, especially the tangential velocity component, was not discussed in detail due to the limitations of the PIV method. Therefore, the turbulent aspects of the tornado-like flow fields are studied systematically via numerical simulations in this section. Herein, the turbulent characteristics are quantitatively examined using the root mean square, rms, of the radial, tangential and axial fluctuating components and the fluctuating surface pressure.

Fig. 11 presents the root mean square of the tangential fluctuating component, v, normalized by V_c. For the weak vortex at $S=0.02$, the tangential fluctuation is very small. When increasing the swirl ratio to the vortex breakdown state, i.e., $S=0.06$, the tangential fluctuation suddenly increases; the profiles exhibit distinct changes. The tangential fluctuations reach a maximum value of $0.8V_c$ at the center and close to the ground. The rms profiles of the tangential velocities in the vortex touch-down state, i.e., $S=0.23$, do not agree with those presented by Ishihara and Liu (2014), especially at very low levels. This difference is because the vortex touch-down stage is a transition stage and is very sensitive

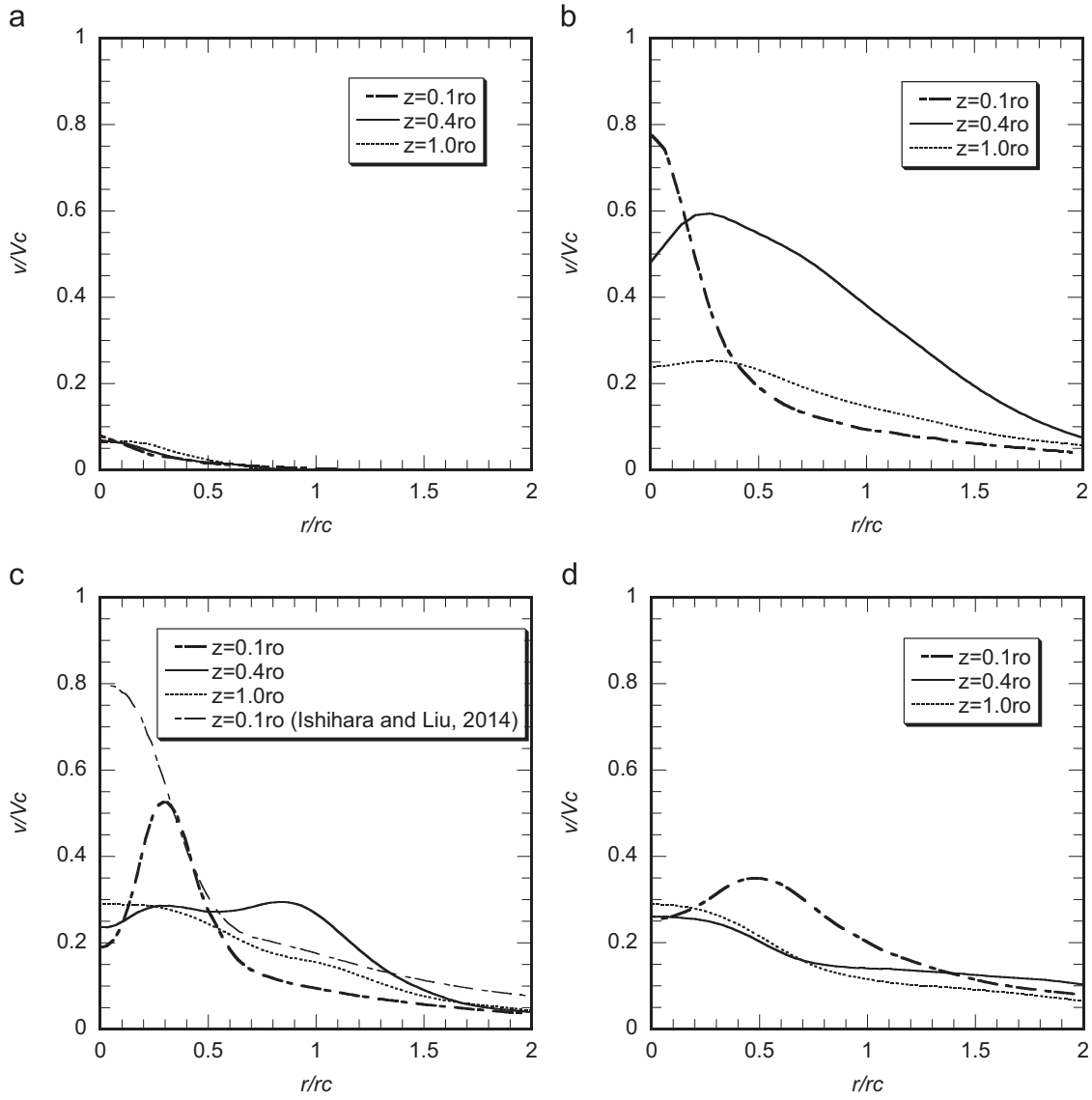

Fig. 11. Radial profiles of the normalized tangential fluctuations for four typical tornado-like vortices: (a) weak vortex, $S=0.02$, (b) vortex breakdown, $S=0.06$, (c) vortex touch-down, $S=0.23$, and (d) multi-vortex, $S=2.44$.

to changes in the swirl ratio. In fact, the situation examined by Ishihara and Liu (2014) was a state between the cases of $S=0.06$ and $S=0.23$. At a height of $z=0.4r_0$, a flat profile of the tangential fluctuation is found, which was described by Ishihara and Liu (2014) to be related to the turbulent bubble that occurs here and significant mixing of the flow. It is found that the tangential fluctuations from the vortex breakdown to the vortex touch-down stages change substantially, although the profiles of the mean tangential velocities are similar; organized swirl motions are a primary source of turbulence production in tornado-like vortices, which was discussed by Ishihara and Liu (2014). By increasing the swirl ratio to the multi-vortex state, the profile of the tangential fluctuation becomes flat at low levels, indicating that the bubble is compressed closer to the surface. At higher levels, i.e., $z=0.4r_0$ and $z=1.0r_0$, the profiles are similar and contain a maximum near the center.

The profiles of the radial fluctuations, u, are plotted in Fig. 12 and are similar to the tangential fluctuations for the weak vortex. The radial fluctuations are not significant, and the maximum fluctuations occur at the center. There is also a sudden change in the radial fluctuations as the swirl rate is increased to $S=0.06$. The maximum radial fluctuation reaches $0.8V_c$ at the center and at a height of $0.1r_0$, which is similar to the tangential fluctuations. By further increasing the swirl ratio to the vortex touch-down stage, the variations in the radial fluctuations with height become gentle except for a very sharp increase near the surface. For the case of $S=2.44$, the radial fluctuations generally increase compared to the vortex touch-down state. The maximum rms of the radial velocities is $0.6V_c$ at $r=0.5r_c$.

Fig. 13 presents the axial turbulence, w. The axial fluctuations change suddenly from the weak vortex to vortex breakdown stages. At the vortex breakdown stage, the axial fluctuations are confined in the expanded recirculation bubble; the maximum axial fluctuation is $1.7V_c$. The tracer particle flow visualization shows that this fluctuation is primarily attributed to the unsteadiness of the breakdown as a function of height. When increasing the swirl ratio to the vortex touch-down stage, the axial turbulence becomes smaller compared to the vortex breakdown stage and the location of the maximum axial fluctuation moves outward. The maximum axial fluctuation occurs at $r=0.5r_c$ and has a value of $0.5V_c$. The axial fluctuations for the case of $S=2.44$ resemble

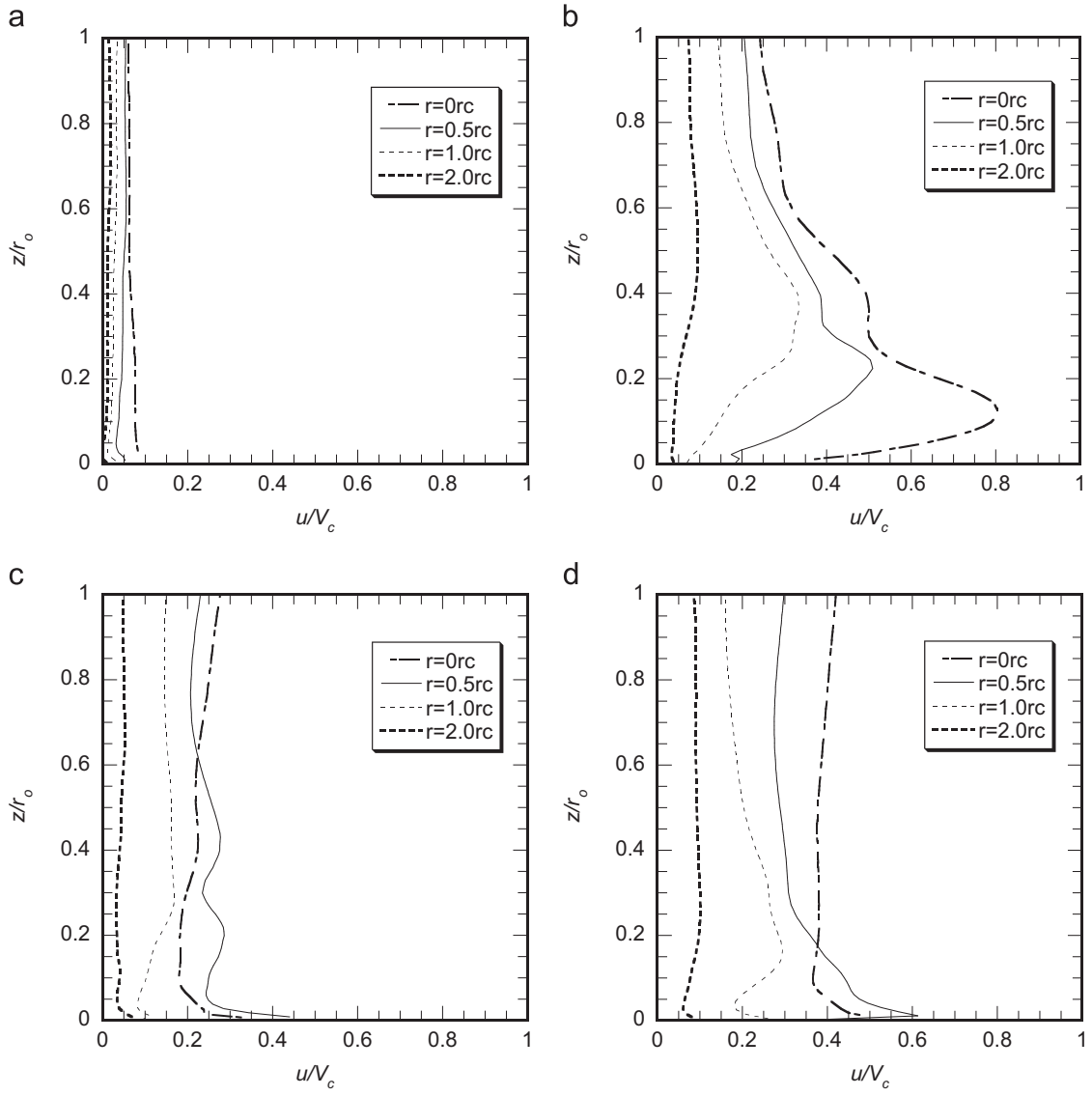

Fig. 12. Vertical profiles of the normalized radial fluctuations for four typical tornado-like vortices: (a) weak vortex, $S=0.02$, (b) vortex breakdown, $S=0.06$, (c) vortex touch-down, $S=0.23$, and (d) multi-vortex, $S=2.44$.

those for the vortex touch-down stage; the maximum axial fluctuation decreases.

To illustrate the surface pressure fluctuations for various tornado structures, Fig. 14 shows the rms of the surface pressure coefficients. For the cases before vortex touch-down, i.e., $S=0.02$ and $S=0.06$, the fluctuations increase when increasing the swirl ratio and exhibit maximum values at the center. By increasing the swirl ratio to the vortex touch-down state, a sharp increase in the fluctuations is found, which is due to the turbulent bubble shifting closer to the surface. Moreover, by further increasing the swirl ratio to $S=2.44$, the radial profile of the pressure coefficient fluctuations becomes flat, which is related to the calm inner sub-core caused by vortex expansion.

3.4. Force balance analysis

Ishihara et al. (2011) investigated the vertical force balance in a tornado-like vortex with a low swirl ratio and the radial force balance for a high swirl ratio using the time-averaged axisymmetric Navier–Stokes equations. Ishihara and Liu (2014) also presented a detailed force balance for the vortex touch-down configuration. A systematic comparison of the force balances in various types of vortices is conducted in this study.

The time-averaged Navier–Stokes equation for the radial force balance can be expressed as follows:

$$U\frac{\partial U}{\partial r}+W\frac{\partial U}{\partial z}-\frac{V^2}{r}=-\frac{1}{\rho}\frac{\partial P}{\partial r}-\left(\frac{\partial u^2}{\partial r}+\frac{\partial uw}{\partial z}-\frac{v^2}{r}+\frac{u^2}{r}\right)+D_u \tag{13}$$

The left-hand side consists of the radial advection term, A_{ru}, the vertical advection term, A_{zu}, and the centrifugal force term, C_r. The right-hand side of the equation includes the radial pressure gradient term, P_r, turbulent force term, T_u, and the diffusion term, D_u. The diffusion term, D_u, in this equation is sufficiently small to be ignored compared with the other terms. However, it is impossible to directly calculate $-V^2/r$, $-v^2/r$ and u^2/r at the central line. A method for calculating these terms was introduced by Ishihara and Liu (2014).

Due to the slight change in the height of the maximum tangential velocity, the terms in the radial momentum equations are computed at $z=0.1r_0$ as a function of r/r_c for all four stages, which is shown in Fig. 15. Fig. 15(a) reveals that turbulence has only a small contribution to the radial momentum balance during the

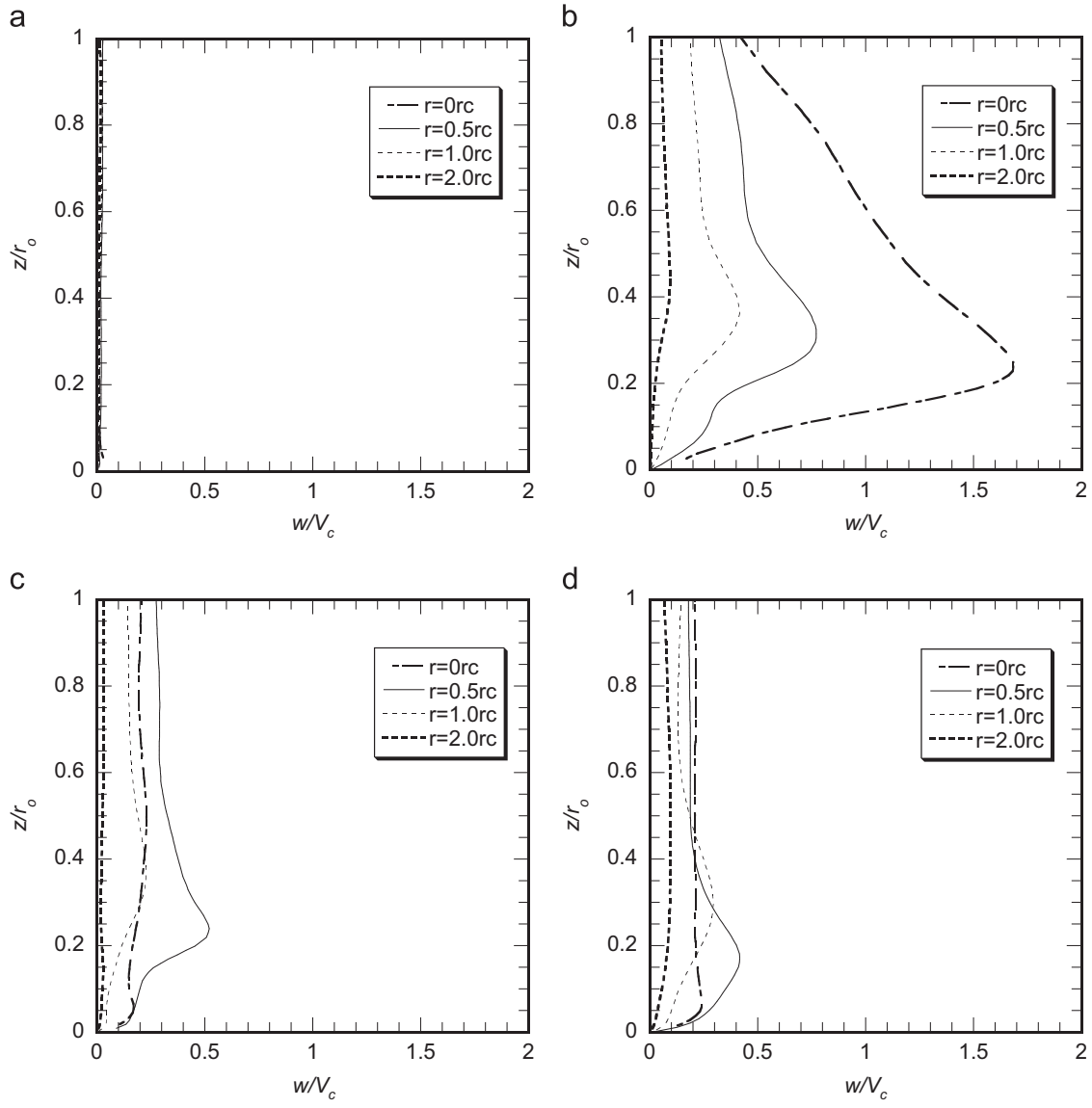

Fig. 13. Vertical profiles of the normalized azimuthal fluctuations for four typical tornado-like vortices: (a) weak vortex, $S=0.02$, (b) vortex breakdown, $S=0.06$, (c) vortex touch-down, $S=0.23$, and (d) multi-vortex, $S=2.44$.

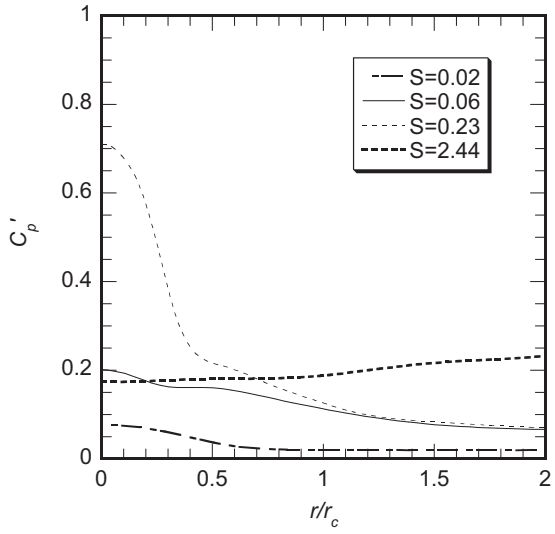

Fig. 14. Radial distribution of the surface pressure coefficient fluctuations.

weak vortex stage. The centrifugal term and pressure gradient term are the significant contributors to the total balance not only in the outer region but also in the core of the vortex, which is where cyclostrophic balance is achieved. By increasing the swirl ratio to $S=0.06$, the flow develops from a laminar vortex to a turbulent state, which is followed by a significant change in the radial force balance (see Fig. 15(b)). The primary balance occurs between the centrifugal term, pressure gradient term, turbulent term and vertical advection term. The magnitudes of the non-zero terms have a similar tendency, i.e., increasing with decreasing radius until reaching a maximum at approximately $r=0.2r_c$ before eventually decreasing to 0 at the center. In the outer region, $r>r_c$, the vertical advection term approaches zero, while the centrifugal term balances only with the pressure gradient term. Fig. 15 (c) displays the terms in the radial balance for the vortex touch-down case. The centrifugal term is primarily balanced by the pressure gradient term and the vertical advection term. However, unlike the vortex breakdown state, the vertical advection term becomes more important than the pressure gradient term in some regions. As for the expansion of the vortex core, the locations with the largest outward shifts occur at approximately $r=0.5r_c$, which

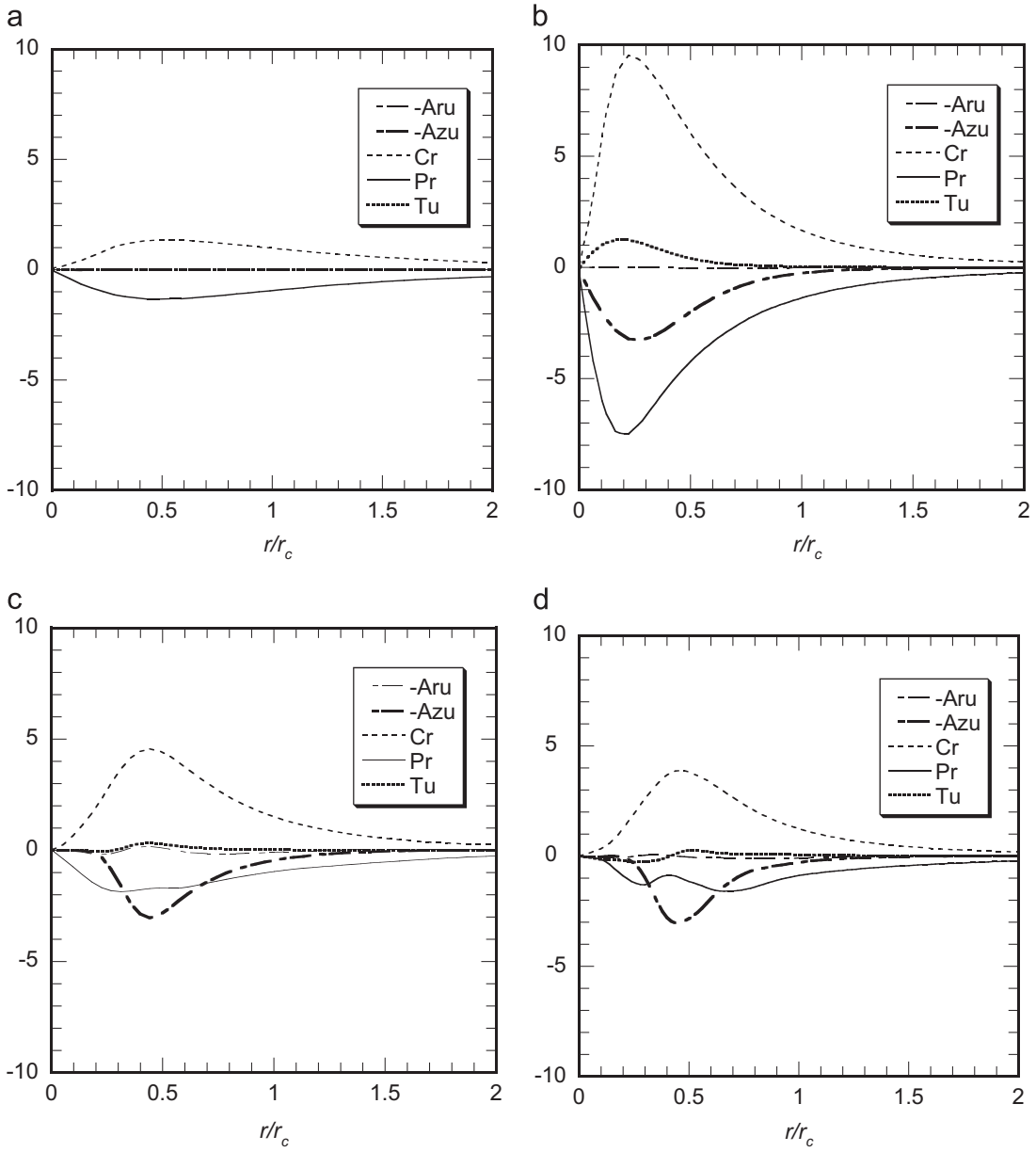

Fig. 15. Radial forces for four typical tornado-like vortices: (a) weak vortex, $S=0.02$, (b) vortex breakdown, $S=0.06$, (c) vortex touch-down, $S=0.23$, and (d) multi-vortex, $S=2.44$.

was also shown by Ishihara et al. (2011). Cyclostrophic balance is also found in the outer region. The radial force balance for the multi-vortex stage is presented in Fig. 15(d), which is almost coincident with that for the vortex touch-down stage. One important observation is that the contribution from vertical advection becomes more significant as the swirl ratio increases. The emergence of turbulence is a manifestation of the unsteadiness of the flow field; however, the turbulent term is not as important as the other non-zero terms for all four stages. The reason in the vortex touch-down case was explained by Ishihara and Liu (2014). They concluded that turbulence in tornado-like vortices is different from turbulence in the fully developed shear layer and that the primary source of the fluctuating horizontal velocities in the tornado-like vortex is the organized swirl motion. The contributions from the fluctuating velocities to the turbulent term nearly cancel each other.

The time-averaged Navier–Stokes equation for the vertical force balance can be expressed as follows:

$$U\frac{\partial W}{\partial r}+W\frac{\partial W}{\partial z}=-\frac{1}{\rho}\frac{\partial P}{\partial z}-\left(\frac{\partial uw}{\partial r}+\frac{\partial w^2}{\partial z}+\frac{uw}{r}\right)+D_w \tag{14}$$

The left-hand side consists of the radial advection term, A_{rw}, and the vertical advection term, A_{zw}. The right-hand side represents the axial pressure gradient term, P_z, turbulent force term, T_w, and the diffusion term, D_w. The diffusion term in the equation is sufficiently enough to be ignored in comparison with the other terms. However, it is impossible to directly calculate $\partial uw/\partial r$ and uw/r at the central line. A method for calculating these terms was introduced by Ishihara and Liu (2014).

Fig. 16 displays the terms in the axial momentum equation at $r=0r_c$. For the weak vortex state in Fig. 16(a), the pressure gradient term exactly balances the vertical advection term, which was also discussed by Ishihara et al. (2011). The radial advection term is zero along the axis, which is related to the symmetry of the mean axial velocity. As shown in Fig. 16(b), the vertical force balance for the vortex breakdown stage exhibits a dramatic evolution

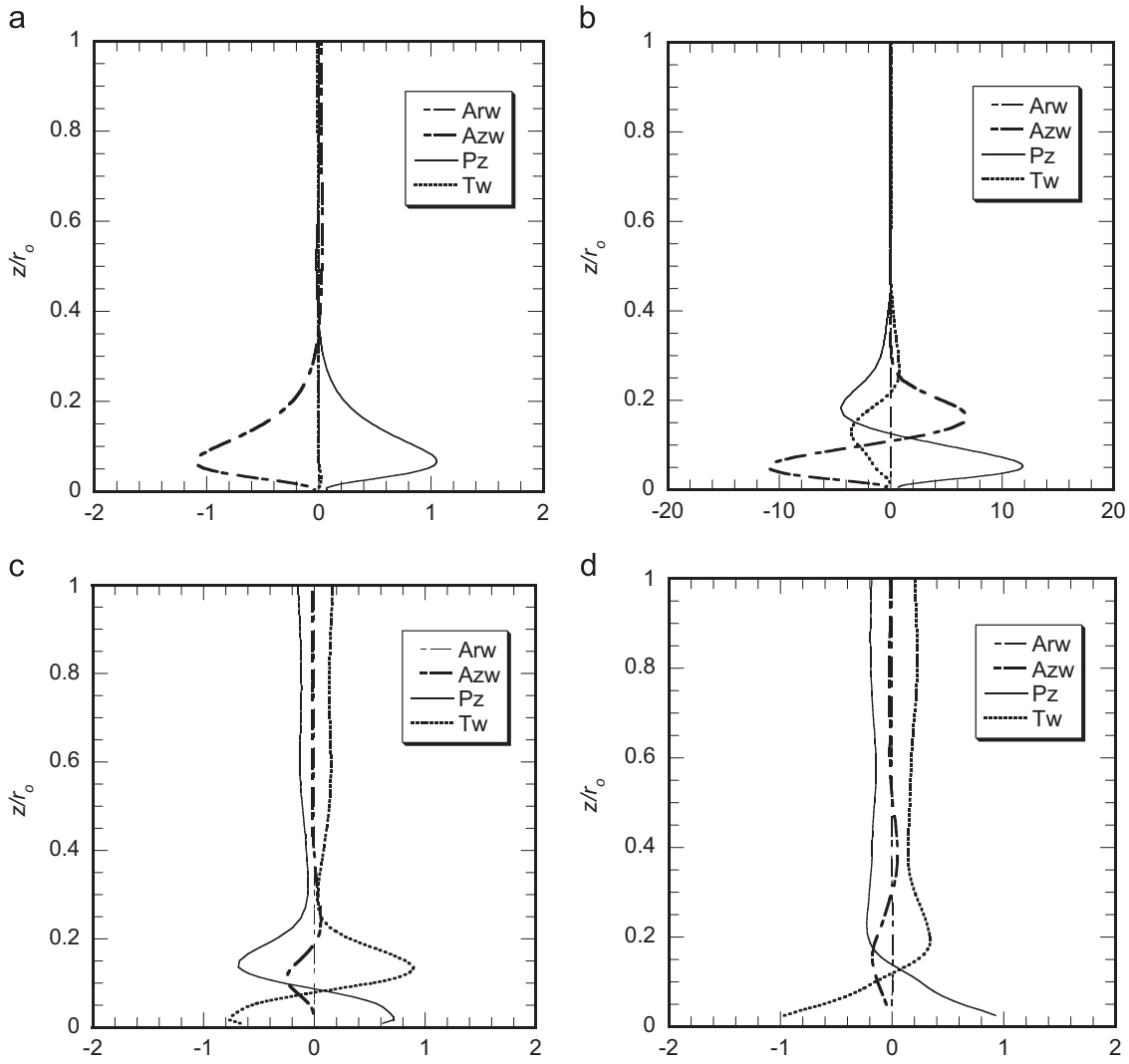

Fig. 16. Vertical force at the vortex centers for four typical tornado-like vortices: (a) weak vortex, $S=0.02$, (b) vortex breakdown, $S=0.06$, (c) vortex touch-down, $S=0.23$, and (d) multi-vortex, $S=2.44$.

compared to the weak vortex. On one hand, the vertical advection term and the pressure gradient term alternate between being positive and negative with height. On the other hand, the turbulent effects reach a maximum contribution at a height of approximately $0.1r_o$. By increasing the swirl ratio to the vortex touch-down stage, the vertical force balance exhibits additional changes (see Fig. 16(c)). Turbulence becomes more important than the vertical advection term and balances with the pressure gradient term. In the multi-vortex case, which is shown in Fig. 16(d), the turbulent term and the pressure gradient term are the primary contributors to the overall balance; these terms reach their maximum values near the surface.

4. Similarity of tornado vortices

In this section, the similarity between the surface intensification and the geometry of tornado vortices is investigated using the local corner swirl ratio. Then, a dimensionless parameter proposed by Hangan and Kim (2008) is adapted to scale the present simulation and to compare with the results from the Spencer tornado.

4.1. Similarity between the surface intensification and the geometry of tornado vortices

A visual approach is adopted to show how the surface intensification and the geometry of tornado vortices changes with the swirl ratio, which is illustrated in Fig. 17. For this purpose, the ratios V_{max}/V_c, $-U_{min}/V_{max}$, W_{max}/V_{max} and $r_{v,max}/h_{v,max}$ are examined. The results of this study are compared with the full-scale numerical study by Lewellen et al. (2000). The methods for determining the angular momentum are different. In this study, the tangential momentum of the inflow is directly obtained from the inlet boundary where the profiles of the tangential velocity and the radial velocity are specified. For the full-scale numerical model by Lewellen et al. (2000), the boundary conditions are obtained from an inner nest of a thunderstorm simulation.

The ratio of the maximum averaged tangential velocity, V_{max}, to the maximum averaged tangential velocity in the upper cyclostrophic region, V_c, is presented in Fig. 17(a) as a function of the local corner swirl ratio. The ratio increases rapidly from very low swirl ratios until S_c is approximately 1.6, which is where vortex breakdown occurs; the peak ratio reaches approximately 1.7. This ratio decreases moderately as the swirl ratio increases to a value of approximately 1.4. Fig. 17(b) shows the ratio $-U_{min}/V_{max}$ as a

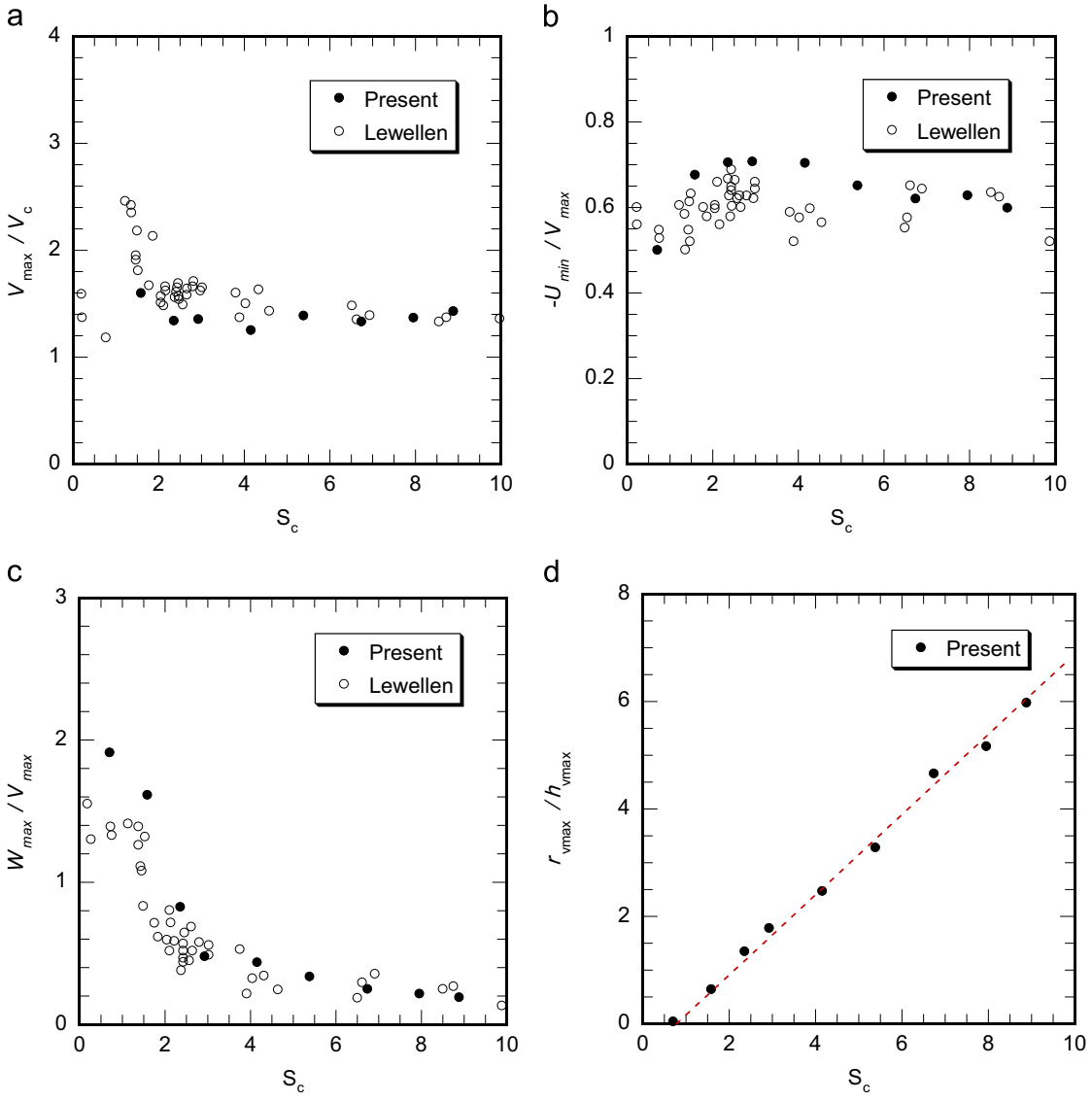

Fig. 17. Summary of surface intensification and the geometry of tornado vortices as a function of the local corner swirl ratio: (a) the ratio V_{max}/V_c, (b) the ratio $-U_{min}/V_{max}$, (c) the ratio W_{max}/V_{max} and (d) the aspect ratio $r_{v,max}/h_{v,max}$.

Table 4
Representative velocities and lengths of the tornado vortices at full scale.

Case name	S_c	U_{min} (m/s)	V_{max} (m/s)	W_{max} (m/s)	$r_{v,max}$ (m)	$h_{v,max}$ (m)	V_c (m/s)	r_c (m)
Case1	0.71	–	–	–	–	–	32.6	26.6
Case2	1.59	−32.3	47.8	77.1	24.7	38.0	29.8	45.6
Case3	2.36	−26.2	37.2	30.8	39.9	30.4	27.7	66.5
Case4	2.93	−28.0	39.6	18.9	51.3	28.5	29.2	89.3
Case5	4.16	−29.2	41.7	18.3	66.5	26.6	33.5	102.6
Case6	5.39	−33.8	52.1	17.3	81.7	24.7	37.8	138.7
Case7	6.74	−35.9	57.9	14.3	104.5	22.8	43.6	159.6
Case8	7.96	−41.7	66.4	14.3	110.2	20.9	48.8	184.3
Case9	8.89	−48.4	81.1	15.2	119.7	19.0	56.7	212.8

function of the local corner swirl ratio. This ratio $-U_{min}/V_{max}$ is insensitive to the swirl ratio; all of the data are scattered around an average value of 0.6. The ratio W_{max}/V_{max} exhibits a maximum value of approximately 1.9 for very low swirl ratios and decreases with increasing swirl ratio, which is depicted in Fig. 17(c). The ratio W_{max}/V_{max} decreases rapidly until the vortex reaches the breakdown state; thereafter, the ratio decreases gradually with increasing swirl ratios.

A vortex aspect ratio, which is defined as the ratio of $r_{v,max}$ to $h_{v,max}$, is applied to evaluate the structure of the flow in the vortex corner. Considering the almost constant thickness of the maximum tangential velocity and the increase in $r_{v,max}$ with the swirl ratio, it is conceivable that the vortex aspect ratio will increase with increasing swirl ratio. The vortex aspect ratio increases linearly with S_c, exhibiting a slope of approximately 0.7 (see Fig. 17(d)).

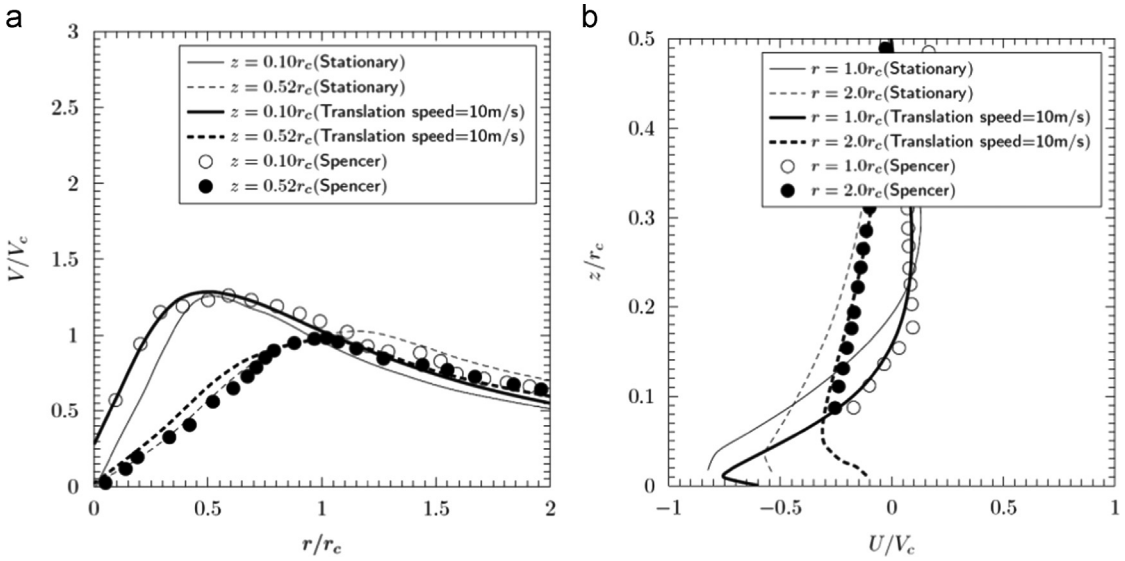

Fig. 18. Comparison of the flow fields between Case9 and the Spencer tornado: (a) tangential velocity and (b) radial velocity.

The values of V_{max}/V_c, $-U_{min}/V_{max}$ and W_{max}/V_{max} as a function of the local corner swirl ratio obtained in Lewellen et al. (2000) are also shown for comparison. Although the present study and the study by Lewellen et al. (2000) use different numerical models to generate the vortices, it is clear that the results from the different models exhibit the same universal tendencies.

4.2. Similarity between the simulated tornadoes and a full-scale tornado

Hangan and Kim (2008) proposed a length ratio, i.e., $r_L = r_{v,max}/h_{v,max,}$ to relate simulated vortices to the full-scale Spencer tornado. The relation is defined between the Spencer tornado with $r_L = 6.0$ and a simulated vortex with $r_L = 6.3$ at $S_c = 8.89$; therefore, the length scale ratio, $r_{max,p}/r_{max,m}$, is 1905, where $r_{max,p}$ is equal to 120 m and $r_{max,m}$ is 0.063 m. Moreover, the velocity scale, $V_{max,p}/V_{max,m}$, is 3.045, where $V_{max,p}$ is 81 m/s and $V_{max,m}$ is 26.6 m/s. The subscripts "$_p$" and "$_m$" represent the values in the Spencer tornado shown by Kuai et al. (2008) and those in Case 9 in this study, respectively. The length and velocity scales are further investigated by comparing the scaled V_c and r_c in Case9 with those for the Spencer tornado. The scaled values are 57 m/s and 213 m in Case9 and 65 m/s and 220 m for the Spencer tornado, which is shown in Table 4.

To verify the aforementioned scaling method, the scaled flow fields for Case9 are compared with those from the Spencer tornado, which were obtained by Haan et al. (2008) using an axisymmetrical model. This axisymmetrical model averages the values at the same radius and height over azimuthal angles. In the present study, the same axisymmetrical model is applied to process the time-averaged data. Fig. 18 shows a comparison of the tangential and radial velocities. For the tangential velocity, the simulated distribution agrees well with that of the Spencer tornado at $z = 0.52r_{c,}$ which is shown in Fig. 18(a). However, near the surface, i.e., $z = 0.1r_c$, there are some discrepancies when no translation is imposed for the simulated tornado, while in the Spencer tornado, the translation speed varies between 10 m/s and 30 m/s based on the analysis of Wurman and Alexander (2005). A comparison of the radial velocity profiles is shown in Fig. 18(b); satisfactory agreement is achieved except for regions near the surface. These discrepancies are almost entirely removed when considering the scaled translation speed of 10 m/s (see Fig. 18), which is equal to 3.3 m/s in the simulation. This is because that even the translation speed was removed in the data set of Spencer tornado, the shape of tornado has become unsymmetrical. As a result when we get the axsymmetrically averaged results, the distortion of the shape of tornado due to the tornado translation will have some effects. For example, when the tornado is stationary, the axsymmetrically and time averaged tangential velocity at the center of the simulator should be 0 as could be found in the data set of simulated stationary tornado in Fig.18(a). If the translation speed is added, the flow fields become unsymmetrical and as a result the axsymmetrically and time averaged tangential velocity at the center becomes nonzero, which is the same as the Spencer tornado. It should be mentioned again that Spencer tornado data published in the study by Haan et al. (2008) are axsymmetrically averaged. The improvement of the comparison of mean tangential velocity and radial velocity by adding a translation speed in the simulation indicates that in order to exactly reproduce the tornado in nature with a translation speed, the translation speed should be taken into consideration as well.

5. Conclusions

The mean and turbulent flow fields and the force balances for four typical tornado vortices are investigated using LES. The similarity between the simulated tornados and a full-scale tornado is examined. The conclusions in this study are summarized as follows:

(1) Four typical tornado vortices, namely, single vortex, vortex breakdown, vortex touch-down and multi-vortex, are successfully simulated using LES. The maximum normalized tangential velocity occurs at the vortex breakdown stage, after which it remains constant to within 21%; the normalized radial location of V_{max} changes only slightly (26%). For the radial velocity, the profiles are similar after the vortex breakdown state; a large portion of the radial flow is concentrated in a thin layer near the surface. Pronounced vertical overshooting is observed in the vortex breakdown state. The vertical overshooting becomes weaker and its location shifts outward for during the vortex touch-down and multi-vortex stages. The maximum pressure drop occurs in the vortex touch-down stage. At the multi-vortex state, the profile of the pressure coefficient is flattened near the center, which is likely related

to the central downdraft touching the ground.

(2) The flow fields in the weak vortex state are laminar. A sudden change in the velocity fluctuations is observed when increasing the swirl ratio to the vortex breakdown stage. By further increasing the swirl ratio to the vortex touch-down stage, the fluctuations decrease, while the maximum fluctuations shift closer to the surface. Hereafter, the fluctuations increase as the swirl ratio increases, and the fluctuation profiles become similar. A sharp increase in the fluctuating surface pressure coefficient is observed in the vortex touch-down state, and the fluctuation profile is flat in the multi-vortex profile.

(3) Turbulence plays a limited role during the weak vortex stage in both the radial and vertical momentum balances. In the vortex breakdown stage, both the force balance changes dramatically and the effects of turbulence emerge. For the vortex touch-down and multi-vortex states, the turbulent term becomes important and is primarily balanced by the pressure gradient term in the vertical momentum balance; the turbulent term in the radial momentum balance is negligible.

(4) A distinct peak in the ratio V_{max}/V_c occurs at approximately 1.7 when vortex breakdown occurs, and V_{max}/V_c becomes nearly constant at 1.4 for the cases with larger swirl ratios. The ratio $-U_{min}/V_{max}$ is insensitive to the swirl ratio, and all of the data are scattered around a central value of 0.6. Moreover, the ratio W_{max}/V_{max} decreases rapidly until the vortex reaches the breakdown state before subsequently decreasing gradually with larger swirl ratios. The height of the maximum tangential velocity is nearly constant. The vortex aspect ratio exhibits a linear relationship with the local corner swirl ratio, having a slope of approximately 0.7.

(5) The scaled flow fields agree well with those for the Spencer tornado when the length ratio for the geometry of the tornado vortex is used to match the simulated vortex to the full-scale vortex of the Spencer tornado. In order to exactly reproduce the tornado in nature with a translation speed, the translation speed should be taken into consideration as well.

References

Alexander, C.R., Wurman, J., 2005. The 30 May 1998 Spencer, South Dakota, Storm. Part I: the structural evolution and environment of the tornadoes. Mon. Weather Rev. 133, 72–96.

Baker, G.L., 1981. Boundary Layer in a Laminar Vortex Flows. (Ph.D. thesis). Purdue University, West Lafayette, IN, USA.

Church, C.R., Snow, J.T., Baker, G.L., Agee, E.M., 1979. Characteristics of tornado-like vortices as a function of swirl ratio: a laboratory investigation. J. Atmos. Sci. 36, 1755–1776.

Ferziger, J., Peric, M., 2002. Computational Method for Fluid Dynamics, 3rd ed. Springer, NY, USA.

Haan, F.L., Sarkar, P.P., Gallus, W.A., 2008. Design, construction and performance of a large tornado simulator for wind engineering applications. Eng. Struct. 30, 1146–1159.

Hangan, H., Kim, J.-D., 2008. Swirl ratio effects on tornado vortices in relation to the Fujita scale. Wind Struct. 11, 291–302.

Ishihara, T., Oh, S., Tokuyama, Y., 2011. Numerical study on flow fields of tornado-like vortices using the LES turbulence model. J. Wind Eng. Ind. Aerodyn. 99, 239–248.

Ishihara, T., Liu, Z.Q., 2014. Numerical study on dynamics of a tornado-like vortex with touching down by using the LES turbulence model. Wind Struct. 19, 89–111.

Kuai, L., Haan, F.L., Gallus, W.A., Sarkar, P.P., 2008. CFD simulations of the flow field of alaboratory-simulated tornado for parameter sensitivity studies and comparison with field measurements. Wind Struct. 11, 1–22.

Lewellen, D.C., Lewellen, W.S., Sykes, R.I., 1997. Large-eddy simulation of a tornado's interaction with the surface. J. Atmos. Sci. 54, 581–605.

Lewellen, D.C., Lewellen, W.S., Xia, J., 2000. The influence of a local swirl ratio on tornado intensification near the surface. J. Atmos. Sci. 57, 527–544.

Lewellen, D.C., Lewellen, W.S., 2007. Near-surface intensification of tornado vortices. J. Atmos. Sci. 64, 2176–2194.

Mishra, A.R., James, D.L., Lethcford, C.W., 2008. Physical simulation of a single-celled tornado-like vortex, Part A: flow field characterization. J. Wind Eng. Ind. Aerodyn. 96, 1234–1257.

Matsui, M., Tamura, Y., 2009. Influence of swirl ratio and incident flow conditions on generation of tornado-like vortex. In: Proceedings of the 5th European and African Conference on Wind Engineering. CD-ROM.

Mitsuta, Y., Monji, N., 1984. Development of a laboratory simulator for small scale atmospheric vortices. Nat. Disaster Sci. 6, 43–54.

Monji, N., 1985. A laboratory investigation of the structure of multiple vortices. J. Meteorol. Soc. Jpn. 63, 703–712.

Nolan, D.S., Farrell, B.F., 1999. The structure and dynamics of tornado-like vortices. J. Atmos. Sci. 56, 2908–2936.

Oka, S., Ishihara, T., 2009. Numerical study of aerodynamic characteristics of a square prism in a uniform flow. J. Wind Eng. Ind. Aerodyn. 97, 548–559.

Rotunno, R., 1977. Numerical simulation of a laboratory vortex. J. Atmos. Sci. 34, 1942–1956.

Tari, P.H., Gurka, R., Hangan, H., 2010. Experimental investigation of tornado-like vortex dynamics with swirl ratio: the mean and turbulent flow fields. J. Wind Eng. Ind. Aerodyn. 98, 936–944.

Ward, N.B., 1972. The exploration of certain features of tornado dynamics using a laboratory model. J. Atmos. Sci. 29, 1194–1204.

Wan, C.A., Chang, C.C., 1972. Measurement of the velocity field in a simulated tornado-like vortex using a three-dimensional velocity probe. J. Atmos. Sci. 29, l16–127.

Wilson, T., Rotunno, R., 1986. Numerical simulation of a laminar end-wall vortex and boundary layer. Phys. Fluids 29, 3993–4005.

Wurman, J., Alexander, C.R., 2005. The 30 May 1998 Spencer, South Dakota, storm. Part II: comparison of observed damage and radar-derived winds in the tornadoes. Mon. Weather Rev. 133, 97–119.